

# The distant Milky Way halo from the Southern hemisphere: Characterization of the LMC-induced dynamical-friction wake\*

MANUEL CAVIERES,<sup>1</sup> JULIO CHANAMÉ,<sup>1</sup> CAMILA NAVARRETE,<sup>2</sup> YASNA ORDENES-BRICEÑO,<sup>3</sup> NICOLÁS GARAVITO-CAMARGO,<sup>4</sup>  
GURTINA BESLA,<sup>5</sup> MAREN HEMPEL,<sup>6</sup> A. KATHERINA VIVAS,<sup>7</sup> AND FACUNDO GÓMEZ<sup>8</sup>

<sup>1</sup>*Instituto de Astrofísica, Pontificia Universidad Católica de Chile, Av. Vicuña Mackenna 4860, 782-0436 Macul, Santiago, Chile*

<sup>2</sup>*Observatoire de la Côte d'Azur, Boulevard de l'Observatoire, 06304 Nice, France*

<sup>3</sup>*Instituto de Estudios Astrofísicos, Universidad Diego Portales, Av. Ejército Libertador 441, Santiago, Chile*

<sup>4</sup>*Center for Computational Astrophysics, Flatiron Institute, 162 5th Ave, New York, NY 10010, USA*

<sup>5</sup>*University of Arizona, 933 N. Cherry Ave, Tucson, AZ 85721, USA*

<sup>6</sup>*Universidad Andrés Bello, Fernandez Concha 700, Las Condes, Santiago, Chile*

<sup>7</sup>*Cerro Tololo Inter-American Observatory/NSF's NOIRLab, Casilla 603, La Serena, Chile*

<sup>8</sup>*Universidad de la Serena, Avenida Cisternas 1200, La Serena, Chile*

## ABSTRACT

The infall of the LMC into the Milky Way's halo impacts the distribution of stars and dark matter in our Galaxy. Mapping the observational consequences of this encounter can inform us about the properties of both galaxies, details of their interaction, and possibly even distinguish between different dark matter models. N-body simulations predict large-scale density asymmetries in the Galactic halo both in baryonic and dark matter due to the passage of the LMC, with the overdensity directly trailing its current orbit through the Southern hemisphere known as the wake. Using the VIRCAM and DECam instruments, we collected wide-field deep near-infrared and optical photometry in four fields chosen to cover the region of the sky expected to span most of the density contrast predicted for it. We identify more than 400 stars comprising two different tracers, near main sequence turn-off stars and red giants, that map the distant halo between  $\sim 60$ –100 kpc, and use them to derive stellar halo densities as a function of position in the sky and Galactocentric radius. We detect (1) a break in the radial density profile of halo stars at 70 kpc that has not been seen in halo studies done from the North, and (2) a clear halo overdensity that starts also at 70 kpc and exhibits a density contrast that increases steadily when moving across the sky into the predicted current location of the LMC wake. If identifying this overdensity with the LMC wake, the peak density contrast we measure is more pronounced than in all available models of the LMC infall, which would indicate the need for a more massive LMC and/or with a different orbit than presently favored. Alternatively, contamination from unidentified substructure may be biasing our detections, so wider-area surveys with similar depth would be needed for confirmation.

*Keywords:* Large Magellanic Cloud (903); Milky Way dynamics (1051); Milky Way dark matter halo (1049); Milky Way stellar halo (1060); Dynamical friction (422); Cold dark matter (265)

## 1. INTRODUCTION

With the advent of space-based proper motion measurements of the LMC/SMC system (Kallivayalil et al. 2006b,a), it has been found that they are most likely on their first passage about the Milky Way (MW, Besla et al. 2007), although the possibility of a secondary passage may hold still (Vasiliev 2024). In a first infall scenario, the impact of the LMC on the MW dark matter (DM) halo will be relatively recent ( $<1$  Gyr), allowing us to probe the imprint of its passage in the stellar halo and potentially test Cold Dark Matter (CDM) theory.

Corresponding author: Manuel Cavieres  
mncavieres@uc.cl

\* Based on observations collected at NOIRLab Cerro Tololo Inter-American Observatory under Chilean TAC program CN2020B-18, and at the European Southern Observatory under ESO programme 109.23H5.001

The LMC is the MW’s most massive satellite, with current mass estimates placing it at about 10% of the MW mass (Besla et al. 2010; Peñarrubia et al. 2016; Patel et al. 2017; Erkal et al. 2019; Erkal & Belokurov 2020; Shipp et al. 2021; Vasiliev et al. 2021; Correa Maganus & Vasiliev 2022; Koposov et al. 2023). Since the seminal work of Chandrasekar (Chandrasekhar 1943), standard theory predicts that the passage of a massive object will create a density wake due to the direct gravitational scattering of the particles in the medium, which in turn acts on the massive body itself, decelerating it by a transfer of angular momentum. This phenomenon, also referred to as dynamical friction (DF), when applied to the passage of the LMC through the MW halo involves both a dark matter wake and a stellar wake counterpart. In this article, we will refer to the stellar wake induced by the passage of the LMC on the MW halo as the *wake*.

The infall of the LMC towards the MW yields several significant effects. Such as the MW’s outer halo reflex motion with respect to the MW–LMC’s barycenter (Gómez et al. 2015; Petersen & Peñarrubia 2021; Erkal et al. 2021; Yaaqib et al. 2024; Chandra et al. 2024); a collective response characterized by a large-scale overdensity leading the LMC, which primarily results from the displacement between the inner and outer halo; a global underdensity that envelops most of the southern hemisphere, encircling the dynamical friction wake, alongside the DF wake overdensity itself (Garavito-Camargo et al. 2019, 2021; Tamfal et al. 2021; Rozier et al. 2022).

Observational evidence of the presence of the wake has been found in the so-called “Pisces overdensity” (Belokurov et al. 2019). First identified as an overdense region in SDSS strip 82 (Sesar et al. 2007), corresponding to the largest overdense region (in volume) after the Sagittarius Stream. Both RR Lyrae and blue horizontal branch (BHB) stars have been observed in the Pisces overdensity (Nie et al. 2015; Watkins et al. 2009; Deason et al. 2018; Belokurov et al. 2019) tracing an elongated shape and distance gradient ranging from 40 kpc up to 100 kpc. Radial velocities of 13 BHB stars with typical halo metallicity in the Pisces Overdensity are consistent with those predicted in Garavito-Camargo et al. (2019), suggesting an association with the stellar wake induced by the LMC (Belokurov et al. 2019).

Additionally, Conroy et al. (2021) reported the detection of the local wake and the collective response using photometry from Gaia Early Data Release 3 (Fabricius et al. 2021; Riello et al. 2021), and infrared photometry from the Wide-field Infrared Survey Explorer (WISE, Wright et al. 2010). Their study comprises

an analysis of 1301 photometrically selected K giants ( $\sim 0.03$  stars/deg<sup>2</sup>) to produce an all-sky density map, revealing an over-density with an apparent amplitude exceeding predictions by numerical models (Garavito-Camargo et al. 2019).

Furthermore, Chandra et al. (2023a) argue that the over-density reported by Conroy et al. (2021) is affected by debris from the LMC and SMC, with at least 20% and up to 50% of the objects being associated with the Clouds. Therefore, an independent detection using more abundant stellar tracers becomes necessary. This will provide a larger, statistically significant trace of the wake and its possible density enhancements along the MW halo, and along the line of sight.

Moreover, the characteristics and density structure of DF wakes are influenced by the physical properties of the medium in which they develop (Ostriker 1999; Furlanetto & Loeb 2002; Lancaster et al. 2020; Vitsos & Gourgouliatos 2023). Consequently, the wake serves as an ideal laboratory for studying the microphysics of DM (see Foote et al. 2023, for a comparison of the wake in fuzzy DM and cold DM). The density and structure of the wake are dependent on both the mass of the LMC and MW, as well as the orbit of the LMC.

In this paper, we report the results of our program for detecting and characterizing the wake through an observational campaign combining both near-infrared and optical photometry. Our data allows us to provide an independent detection of the wake, as well as a detailed view of the specific density enhancement at different heliocentric distances. Based on the observed density enhancements, we compare with existing simulations of the LMC-MW interaction, which allows us to place constraints on the virial mass at infall of the LMC.

This paper is structured as follows: in Section 2 we describe the observations, data reduction procedures, and photometry methodologies. Section 3 describes the selection criteria utilized to identify the halo tracers used, as well as the methodology utilized to derive photometric distances. In Section 4 we present our derived halo density profiles and their comparison with simulations. The discussion about the impact of other stellar substructures and its implications takes place in Section 5. We conclude in Section 6.

## 2. OBSERVATIONS AND DATA PROCESSING

The primary observational data used in this paper were collected as part of a photometric campaign carried out during 2020 at the CTIO 4m Blanco telescope with the Dark Energy Camera (Flaugher et al. 2015, DECam) along with data collected using the Visible and Infrared Survey Telescope for Astronomy (VISTA; Emerson et al.

2006) and the VIRCAM instrument (Dalton et al. 2006). We observed 4 fields to which we will refer by their tile number from 1 to 4. The pointing coordinates are at DEC = 0 deg, RA = 334.9, 343.0, 359.0, 7.0 deg, and were defined to approximately cover the entire density range of the wake according to current numerical models of the LMC-MW interaction (Garavito-Camargo et al. 2019) and also probing the overdensity known as the Pisces Overdensity (Belokurov et al. 2019; Conroy et al. 2021). Figure 2 presents the locations of the 4 observed fields overlaid on a density map of DM particles from Garavito-Camargo et al. (2019). For convenience, the location of the observed fields was placed along the celestial equator (dotted grey line in Figure 2) as it is approximately perpendicular to the expected past orbit of the LMC shown as a black line in Figure 2.

DECam observations were performed during the nights of the 9th to the 12th of November 2020, with additional exposures being performed during the 23rd of November, 2020. The strategy for DECam data acquisition was to maximize the signal-to-noise ratio for faint sources while keeping overheads to a minimum. For this purpose, all exposures for the  $g$  and  $i$  bands were performed during dark time, integrating on-source for 3600 and 4800 seconds on  $g$  and  $i$ , respectively, split into 10-minute exposures, amounting to a total of about 10 hrs of integration time, or 2.5 hours per field. The seeing of our DECam observations varied between  $0''.58$  and  $1''.04$  with median values of  $0''.68$  in  $g$  and  $0''.94$  in  $i$ . Airmass values had a minimum of 1 and a maximum of 1.59 with a median of 1.24 in  $g$  and 1.15 in  $i$ .

To maximize the signal-to-noise ratio for faint sources, we chose to only perform a ‘line-dither’ pattern with offsets of 5 arcseconds on our DECam observations. Consequently, the resulting spatial coverage did not fill the gaps between detectors but still allowed for the interpolation of bad pixels, and resulted in a larger effective exposure time for the stacked images at the expense of losing coverage of the gaps.

Near-infrared VIRCAM observations took place between the 2nd of June 2022 and the 25th of November 2022. Observations were performed in the  $K_s$  band with a 7-second detector integration time following a 12-exposure ‘jitter3u’ pattern, resulting in 84 seconds of integration time per individual detector frame stack called *pawprint*. We followed the standard 16-pawprint scheme to fill the gaps between the 16 detector chips, resulting in a  $1.6\text{deg}^2$  field comparable to the field of view of one DECam image. In total, we observed 2516 pawprints for our 4 fields, amounting to 58.7 hrs of integration time, which corresponds to  $\sim 14.7$  hours of integration time per field. The airmass for our  $K_s$  ob-

servations ranged from 1.1 to 1.723, with a median of 1.22. The seeing during our VIRCAM observations was typically excellent, with a median value of  $0''.8$  and individual exposures presenting a range of seeing from  $0''.57$  to  $0''.99$ .

### 2.1. Image processing

The DECam data was processed using the NOAO Community Pipeline (Valdes et al. 2014), which generated the stacked images. However, due to the large exposure times, many of our observations were affected by prominent satellite trails. To address this before performing photometry, we first applied a 15-pixel median blur to minimize noise. This was followed by the application of a Canny filter (Canny 1986) for edge detection. The edge-detected image was then converted into a binary format using an adaptive Gaussian threshold. This threshold was calculated as the weighted sum (cross-correlation with a Gaussian window) of the  $11 \times 11$  pixels neighborhood around each pixel  $(x,y)$ , manually tuned by subtracting 2. Subsequently, a probabilistic Hough transform (Matas et al. 2000) was used on the binary image to identify lines with a minimum length of 100 pixels and a maximum line gap of 50, with all identified lines being masked in the weight maps of each stacked image. For VIRCAM observations, all pawprints that show satellite stripes were removed.

Our analysis of the VIRCAM data is largely based on the standard data products provided by the VISTA Data Flow System (VDFS; Emerson et al. 2004) run by the Cambridge Astronomy Survey Unit (CASU) using a pipeline described by Irwin et al. (2004) and regularly updated until the decommissioning of the instrument. We primarily focused on the processed pawprints, which have already undergone a dark subtraction, rest anomaly rectification, flat-fielding, initial sky-subtraction, de-stripping, non-linearity corrections, and gain normalization (Irwin et al. 2004), thereby eradicating most of the signature of the instrument. Pawprints are then resampled using *swarp* (Bertin et al. 2002) with a LANCOZ3 kernel. This resampling method enhances image resolution through interpolation and smoothing, while concurrently functioning as a low-pass filter. This filtering process effectively eliminates some of the low-frequency components of the image that correspond to large-scale structures, such as background variability, aiding in the detection of point sources.

For the deep stacking of VIRCAM pawprints, we chose to bypass the VDFS tiles due to known issues with deep stacked images (see Meingast et al. 2016). Consequently, the coaddition of pawprints was carried out using *swarp* (Bertin et al. 2002), employing a clipped combination

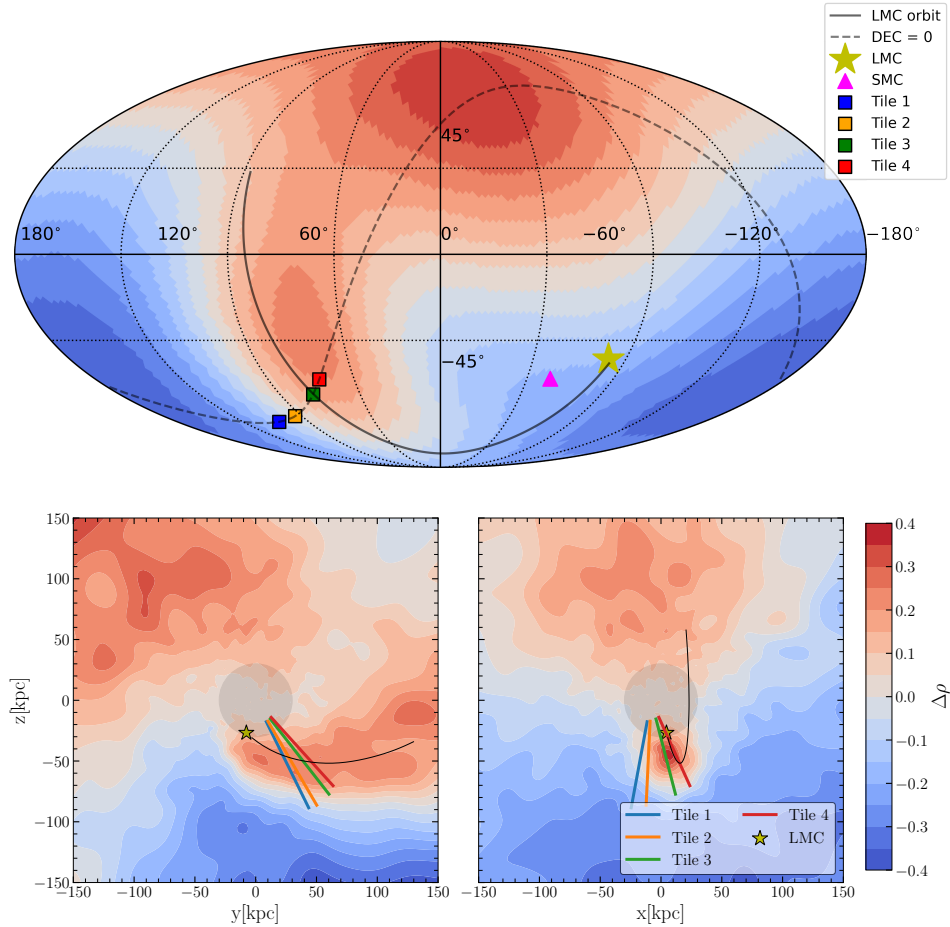


**Figure 1.** The upper panel shows the all-sky Aitoff projection map of simulation particles (at Galactocentric distances in the range  $60 \text{ kpc} < R_{\text{GC}} < 100 \text{ kpc}$ ) from Garavito-Camargo et al. (2019) models of the LMC-MW interaction. Displayed in blue-to-red is the dark matter particle density for a Garavito-Camargo et al. (2019) simulation that includes the interaction between the LMC and MW-halo. Density is computed as the number of particles found per square degree based on the fifth-level HEALPix tessellation system smoothed with a 15-degree kernel. The lower panels show the projected DM density in the Galactocentric plane at  $x = 0$  on the left and  $y = 0$  on the right, both with a thickness of 10 kpc. The overdensity in the north is the collective response of the Galactic halo, while the overdensity found in the southeast region corresponds to the wake. Our observed fields are shown as squares and lines in blue, yellow, green, and red, corresponding to Tile 1, 2, 3, and 4. The SMC and LMC are shown as a magenta triangle and yellow star, respectively, for reference purposes. The past orbit of the LMC obtained from Garavito-Camargo et al. (2019) is shown as a black line, and the celestial equator is shown as a dotted grey line. It can be clearly observed that, when comparing the density across our observed fields, we expect to find a density enhancement both along the line of sight, as shown in the lower panels, and in projection, as shown in the upper panel.

algorithm. This algorithm conducts outlier detection on each input image to create a mask, after which it performs a median combination, effectively mitigating issues related to ghosting and cosmic ray impacts. Unlike the typical approach of constructing a median stack, the clipped or outlier-filtered mean stacked point-spread function (PSF) comprises a linear combination of the single frame PSFs, provided that the different PSFs are moderately homogeneous which we impose during the seeing selection. This characteristic is particularly crucial for model-fitting photometry (Gruen et al. 2014).

## 2.2. Photometry

Photometry was carried out using a combination of *SExtractor* and *PSFex* (Bertin & Arnouts 1996; Bertin 2011). The process began with image segmentation to establish an accurate detection threshold, focusing exclusively on areas of the stacked image covered by one of the detectors. This step is crucial as the gaps between chips can artificially lower the standard deviation estimates made by *SExtractor*. The segmentation process considered only pixels that exceed the threshold set by the SKYSUB keyword in the image header. Subsequently, the standard deviation was calculated after performing five iterations of sigma clipping, using a  $5\sigma$  limit, thus



not including obvious sources in the detection calculations.

Moving to source detection, sources exceeding 1.5 standard deviations across more than 3 pixels were identified, with their positions, ellipticity, FWHM, and fluxes being measured. All sources meeting the criteria of *SExtractor*  $|FLAG| = 0$ ,  $SNR > 20$ , ellipticity  $< 0.3$ , and a separation of at least 35 pixels from other sources (equivalent to angular separations of 9.2 and 11 arcsec in DECam and VIRCAM, respectively), were then processed by *PSFex*. This step involved modeling a non-parametric, spatially variable PSF model, which was subsequently utilized for the final PSF photometry with *SExtractor*. In the final photometry, the previously computed PSF model was used to measure the position, instrumental magnitudes, and fluxes of all sources exceeding 1 standard deviation across more than 3 pixels.

The computation of individual zero-points was carried out as follows. Initially, point-like sources were selected using the *SExtractor* `SPREAD_MODEL` parameter. This parameter represents a morphometric linear discriminant, obtained from the fitting of a Sérsic model, and is employed following the prescription provided by Koposov et al. (2015). This method, being noise-dependent, offers robustness against variations in the signal-to-noise ratio (SNR) of sources. The specific criterion used is shown in Equation 1.

$$|\text{SPREAD\_MODEL}| < 0.003 + \text{SPREADERR\_MODEL} \quad (1)$$

In the second step, to circumvent issues with saturation, we only considered sources with instrumental magnitude `MAG_PSF` fainter than 18 for the *g* and *i* bands, and fainter than 13 for the  $K_s$  band. To avoid low SNR sources we required that the *SExtractor* parameter `MAGERR_PSF`  $< 0.01 \text{ mag}$ .

The third step involved an on-sky crossmatch with a 1" tolerance for magnitude comparison. For the *g* and *i* bands, the external catalog used was the Sloan Digital Sky Survey DR16 catalog (SDSS; Ahumada et al. 2020), and for the  $K_s$  band, the UKIRT Infrared Deep Large Area Survey (UKIDSS; Lawrence et al. 2013) was chosen as the external reference.

Finally, the zero-point was calculated as the mean difference between the reference magnitudes (from the external catalogs) and the instrumental (`MAG_PSF`) magnitudes.

Completeness tests were carried out separately for each filter. The artificial stars used in the completeness tests were defined by a 2D Gaussian with FWHM corresponding to the specific seeing of each stacked image. The completeness value for a given magnitude was calcu-

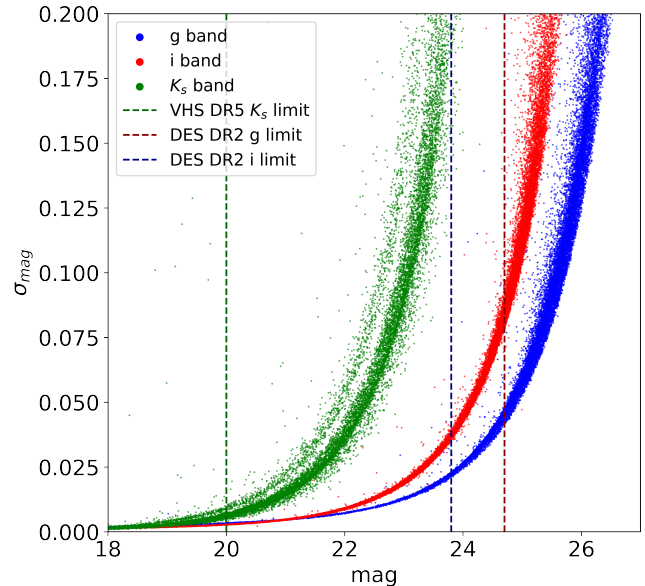


**Figure 2.** Photometric uncertainties of point sources in our VIRCAM/DECam stacked images as a function of magnitude.  $K_s$  band uncertainties are shown in green, *g* and *i*-band uncertainties are presented in blue and red. The 90% limiting magnitude for current surveys that present coverage of the region are shown as vertical dashed lines in green for the  $K_s$  band in the VHS survey; blue and red for the *g* and *i* band limits in DES DR2.

lated by adding approximately 10000 artificial stars with magnitudes ranging between 22 and 29, and then running the same photometric pipeline as used for the data (e.g. detection, aperture photometry, PSF fitting, and final PSF photometry). The final completeness value is then the magnitude at which the percentage of the recovered input stars reaches 90% and is an average of 24.8 mag in the *i*-band, 25.8 in the *g*-band, and 24.37 mag in the  $K_s$  band (AB system).

Figure 2 presents the photometric uncertainties for point sources detected at 1-sigma in our stacked images across all three bands (*g*, *i*, and  $K_s$ ). The depth of our data is evident when comparing our photometric uncertainties with those of surveys covering the same region. The 90% completeness limits of these surveys are shown in Figure 2 as dashed lines, in green for the VISTA hemisphere survey (VHS; McMahan et al. 2013)  $K_s$  band; in blue and red for the *g*, and *i* band photometry of the second data release of the Dark Energy Survey (DES, Abbott et al. 2021).

### 2.3. Extinction

Considering the low Galactic latitude of the observed fields, the extinction associated is quite low. However, there is significant differential reddening within and be-

tween each observation tile, attributable to the vast area they cover.

The extinction correction was implemented using the re-calibrated map by Schlafly & Finkbeiner (2011), originally developed by Schlegel et al. (1998) with coefficients for the  $g$ ,  $i$  and  $K_s$  bands obtained from Table 6 of Schlafly & Finkbeiner (2011).

#### 2.4. Star/Galaxy separation

The star-galaxy separation process harvests the particular behavior of stars in the  $giK_s$  color-color diagram displayed in Figure 3, where different stellar and galaxy populations can be recovered (Ordenes-Briceño et al. 2018). From redder to bluer colors in the  $(i - K_s)$ -axis: the bulk of the population of star-forming galaxies having  $(i - K_s) \sim 1.0$  mag and bluer  $(g - i)$  colors, while passive galaxies are found with slightly bluer colors, having mainly  $0.0 < (i - K_s) < 1.0$  mag. The stars, on the other hand, occupy a thin locus, with significantly bluer  $(i - K_s)$  colors than galaxies and a wider range of  $(g - i)$  colors. This separation in color-color space from galaxies resembles the one recovered in Muñoz et al. (2014) using  $(u - i)$ ,  $(i - K_s)$  color-color space and it is the result of the wide spectral energy distribution covered by the three filters.

To select stars, only point source-like detections are considered based on their morphology (i.e., satisfying the criterion of Equation 1). After that, the star selection procedure is a two-step process: initially, a wide selection of the stellar locus was made aiming to isolate it, avoiding as much as possible the contamination from galaxies while maintaining high completeness of the stellar locus and discarding largely discrepant sources at redder  $(i - K_s)$  colors. These limits are shown as straight red dashed lines in Figure 3 and correspond to the polynomial:  $i - K_s = 0.61(g - i - 2) + 0.8$  and  $i - K_s = 0.61(g - i - 2) - 0.5$ . After the initial cut, a 6-degree polynomial is fitted to the fiducial stellar locus, described in equation A1 and presented as a blue line on Figure 3. The data is then partitioned into 50 bins along the  $g - i$  axis; in each bin, only sources residing within a  $1.5 \sigma$  distance from the polynomial fit are incorporated. The final star selection is illustrated as orange points in Figure 3. This particular selection was chosen to minimize contamination from background galaxies, which sacrifices completeness towards redder colors where red dwarf populations are expected.

The results of this procedure are shown in the Hess diagram (i.e., the density of sources in the color-magnitude space) in Figure 4: the left panel presents point sources from all tiles amounting to 170 635 objects, where an increased number of sources have  $g$ -band magnitudes

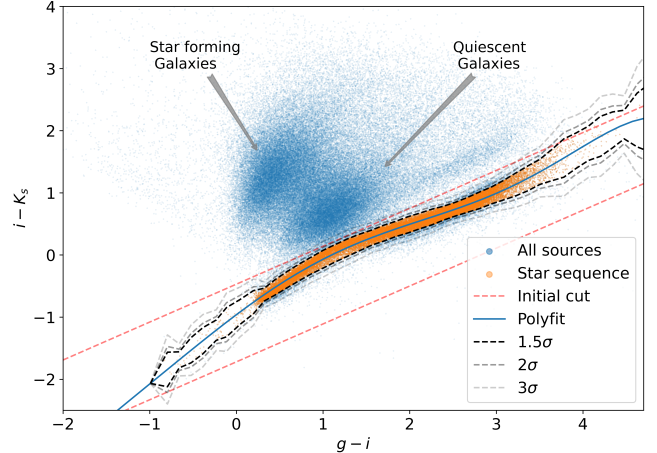


**Figure 3.**  $g - i$  vs  $i - K_s$  diagram, to which we will refer to as the  $giK_s$  diagram. The stellar locus corresponds to the lower sequence stretching from  $(g - i) \sim 0.0$  to  $(g - i) \sim 4$  mag. Star selection is shown in orange and corresponds to sources found within  $1.5 \sigma$  from the fitted polynomial (blue solid curve). Sources found in the group centered about  $(g - i, i - K_s) = (1, 0.7)$  mag corresponds to quiescent galaxies, while the cloud centered at  $(0.5, 1.3)$  mag corresponds to star-forming galaxies.

fainter than 23 mag, stressing the need for an effective star/galaxy separation. After removing galaxies as described above, in the middle panel we show that there are 31 872 stars from all tiles, where the effect of non-resolved galaxies becomes evident as they occupy the same color and magnitude space as stars in the CMD; the right panel shows the sources removed as a result of the star/galaxy separation procedure, which corresponds to 138 763 objects (i.e.,  $\sim 81.3\%$  of the total point sources).

### 3. HALO TRACERS

#### 3.1. Red Giant Branch Stars

To construct a methodology for selecting red giant branch (RGB) stars with the available photometry ( $g$ ,  $i$ , and  $K_s$  bands), we need to know where different evolutionary sequences lie in the  $giK_s$  color-color diagram. To guide our selection we used data from the Sloan Extension for Galactic Understanding and Exploration 2 (SEGUE, Rockosi et al. 2022). This survey provides low-resolution spectra ( $R \sim 1800$ ) for 118 958 stars, prioritizing distant halo tracers such as BHBs, K giants and M giants. Additionally, SEGUE provides the derived fundamental parameters for each object, allowing for an unequivocal selection of RGB stars in the Kiel diagram shown in panel a) Figure 5.

The SEGUE reference sample of RGB stars is defined to be all objects that fall within the polygon defined by the following points:  $(T_{\text{eff}}, \log(g)) = (4923, 1.98)$ ,  $(4894,$

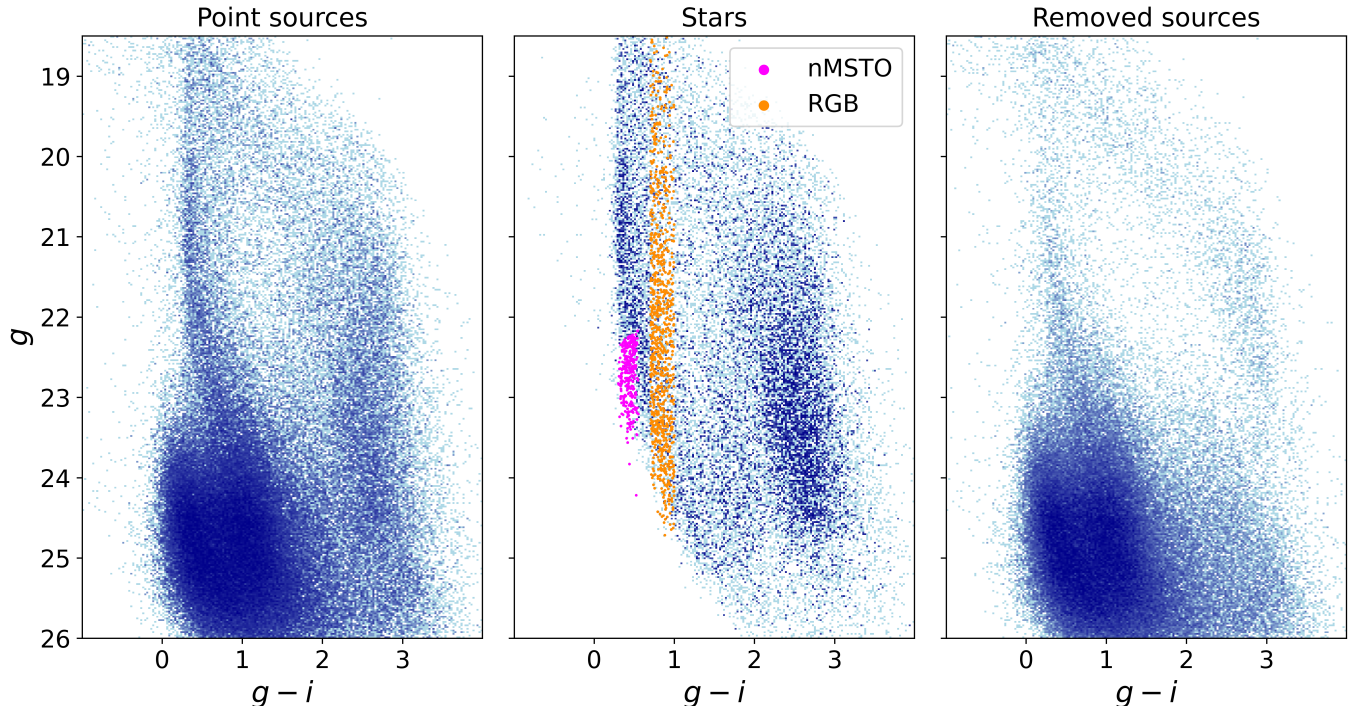


**Figure 4.** The left panel presents the color-magnitude diagram of point sources in blue. The central plot highlights the selected stellar sources. The nMSTO and RGB samples are shown in magenta and orange respectively. The right panel shows the sources that were removed through the star-galaxy separation procedure applied to point sources. The efficacy of the star-galaxy separation procedure is evident in this arrangement. The removed sources, predominantly comprising non-resolved sources such as galaxies or single stellar populations, occupy a significant portion of the parameter space and dominate the counts at  $g \geq 22$ , thus overlapping the nMSTO and RGB selection at large distances.

1.87), (5039, 1.84), (5088, 1.88), (5216, 2.25), (5294, 2.48), (5317, 2.55), (5399, 2.81), (5418, 2.87), (5460, 3.02), (5467, 3.04), (5467, 3.06), (5451, 3.11), (5278, 3.14), and it is presented on Figure 5.a as the orange selection. The SEGUE RGB selection was chosen to prioritize low contamination at the expense of completeness, thus limiting to the center of the RGB locus shown in panel a) on Figure 5.

We crossmatch all SEGUE stars with  $g$  and  $i$  photometry from SDSS and  $K_s$  photometry from the ninth data release of the UKIDSS Large Area Survey (Lawrence et al. 2013). This allows us to plot them in the  $giK_s$  diagram shown on Figure 5.b to trace the spectroscopic sample of SEGUE RGB stars into the  $giK_s$  diagram. We find that the majority of our SEGUE reference sample occupies a sequence in the  $giK_s$  space, shown as orange dots on Figure 5.b.

By coloring the SEGUE stars by their metallicity in the  $giK_s$  diagram, we found that stars with low metallicity ( $[M/H] < -1.3$ ) lie in a distinct part of the stellar locus, shifting to higher  $i - K_s$  colors. To test if this is not a feature of the SEGUE data alone, we also performed a crossmatch of data from the 8th data release of the Large Sky Area Multi-Object Fiber Spectroscopic

Telescope (LAMOST; Cui et al. 2012) survey, medium resolution spectra with SDSS and UKIDSS photometry. We then plotted all LAMOST stars in the  $giK_s$  diagram, colored by metallicity. A robust locally-weighted regression, based on the implementation by Cappellari et al. (2013) of the algorithm by Cleveland & Devlin (1988), was applied to highlight the larger behavior of the data and reduce noise. The result of this procedure is shown in Figure 5.c, where a clear metallicity gradient is observed as a diagonal vector towards redder ( $i - K_s$ ) and bluer ( $g - i$ ) colors. This effectively makes it possible to separate low metallicity RGB stars from the main sequence by only utilizing the  $g$ ,  $i$ , and  $K_s$  bands. Particularly, this hints at a dependency between the  $i - K_s$  color of the RGB and the metallicity of the stellar population.

Guided by the SEGUE RGB reference sample described above, we select RGB stars from our VIRCAM/DECAM data set by first imposing the criteria:  $0.7 \leq g - i \leq 1$  mag, following the color range of the SEGUE RGB sample (orange points in Figure 5.b). Secondly, we required stars to have a perpendicular distance smaller than 0.035 mag from the RGB sequence of a PARSEC (Bressan et al. 2012) isochrone of 10 Gyr and



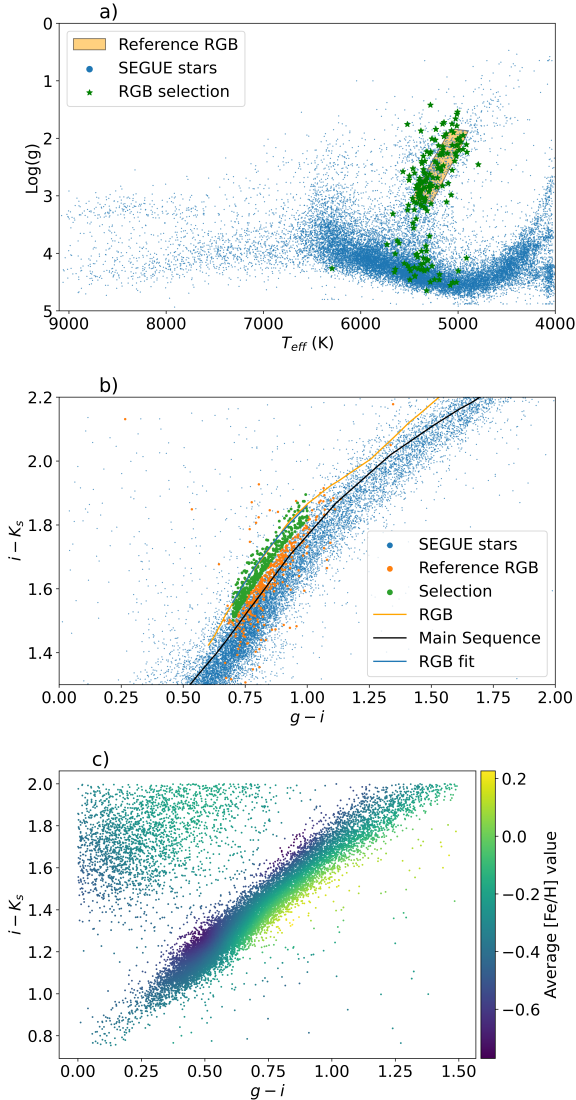


**Figure 5.** a) Kiel’s diagram/spectroscopic HR diagram shows the logarithm of surface gravity ( $\log(g)$ ) as a function of the effective temperature ( $T_{\text{eff}}$ ) for SEGUE-2 stars using SDSS and UKIDSS photometry. The adopted selection of RGB stars is shown as an orange polygon (see the main text). Stars meeting the RGB selection criteria in the  $giK_s$  diagram are marked as green stars, highlighting the main sequence contamination evident from 23.1% of stars with  $\log(g) > 4$  within the RGB selection. b) The  $giK_s$  color-color diagram displays all stars in blue, giants selected on the Kiel diagram (orange polygon in the left panel), and the RGB selection in green. The RGB and main sequence for a 10 Gyr,  $[M/H] = -1.5$  [M/H] isochrone are depicted in orange and black, respectively. c)  $giK_s$  color-color diagram of LAMOST DR8 stars having DES and UKIDSS photometry, colored by metallicity showing the metallicity gradient present in the stellar locus, allowing for the separation of low metallicity ( $[M/H] < -0.6$  dex) RGB stars from the main sequence. A robust locally weighted regression has been applied to display the broad tendency and reduce noise.

$[M/H] = -1.5$  dex, shown as an orange line on Figure 5.b. This specific distance criterion was chosen to ensure the stars’ separation exceeded the average photometric uncertainty vector (ie, considering  $g - i$  and  $i - K_s$  color uncertainty) from the main sequence (MS) and to select stars with typical halo metallicities (ie within a  $-1.3$  dex to  $-2.3$  dex range).

Additionally, to remove potential foreground sources, we cross-match our sample with the Third Data Release of the Gaia mission (Gaia Collaboration et al. 2023), and impose the condition in parallax  $\pi < 0.1$  mas (distances greater than  $\sim 10$  kpc), effectively filtering out 327 bright foreground objects from the initial 1261 sources.

We evaluated the performance of our RGB selection criteria by reapplying them to SEGUE-2 stars in the  $giK_s$  diagram and checking on the Kiel’s diagram if they lie in the RGB. The selected stars are shown as green dots on Figure 5.b and as green stars on the Kiel diagram shown in Figure 5.a. Considering stars with  $\log(g) > 4$  as main sequence contaminants (Angelov 1996), yields a precision of 77.9%, with 23.1% of the stars having  $\log(g) > 4$ .

Applying this selection criteria to our photometric catalog yields a total of 934 giants in our 4 fields, which amounts to  $\sim 142$  stars/deg<sup>2</sup>.

### 3.2. Near main sequence turn off stars

The second tracer available in our photometry is Near Main Sequence Turn-Off (nMSTO) stars, which are significantly more abundant than other typical halo tracers, such as RR Lyrae, BHB stars, and K giants. nMSTO stars are the faintest halo tracers reached by our photometric catalogs. Considering the completeness limit of our data, such stars can be identified up to a distance of 100 kpc. This tracer has been widely used to probe the outer halo (Chen et al. 2001; Jurić et al. 2008; Bell et al. 2008; Sesar et al. 2011) as their larger abundance allows to place competitive limits on the global density profile and shape of the Galactic halo with a relatively small number of narrow fields of view (Pila-Díez et al. 2015).

To select nMSTO stars, we used the selection criteria performed in Pila-Díez et al. (2015) as a reference to devise a selection method using the  $g$ ,  $i$ , and  $K_s$  bands. Their selection is based on the  $u$ ,  $g$ ,  $r$ , and  $i$  photometry, by applying two empirical photometric variables. The first is the metallicity  $[Fe/H]$ , which is determined using Bond et al. (2010) photometric metallicity relation based on SDSS spectroscopic metallicity. The second empirical variable is the absolute magnitude  $M_r$ , derived from Ivezić et al. (2008) photometric parallax relation,



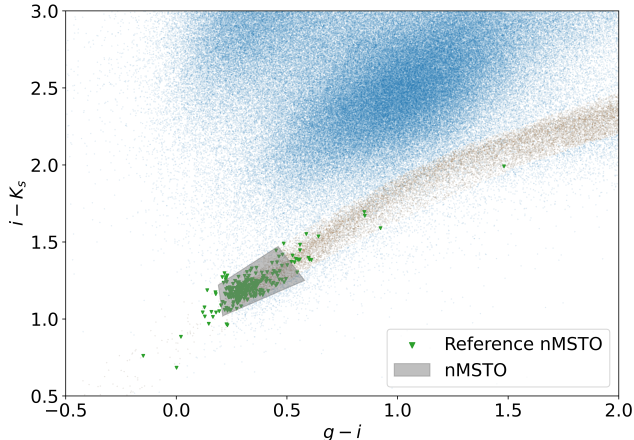


**Figure 6.**  $giK_s$  diagram showing point sources in blue, while stars shown in orange. Green triangles correspond to the reference selection of nMSTO stars given by Pila-Díez et al. (2015) criteria plotted using DES and UKIDSS photometry. Our polygon for defining nMSTO stars is shown as a grey box.

which was calibrated from globular clusters with known distances in SDSS data. The resulting color limits are shown in equations 9 to 13 in Pila-Díez et al. (2015).

By applying Pila-Díez et al. (2015) criteria on the photometry from DES we obtained a reference sample of nMSTO stars. The use of DES photometry is essential, as it provides photometry across all the bands used by Pila-Díez et al. (2015). This reference sample is then matched with UKIDS photometry by a crossmatch with a tolerance of 1 arcsecond. This provides a sample of nMSTO stars with  $giK_s$  photometry, which we show in Figure 6 as green triangles.

The selection box for nMSTO stars in our photometry is given by the following box:  $(g - i, i - K_s) = (0.21, 1.02), (0.19, 1.22), (0.46, 1.47), (0.58, 1.25)$ . This particular box was chosen to cover most of the reference sample, excluding outliers. Contamination is expected to be low within this box, since in the  $giK_s$  color-color diagram old (10 Gyr or more) isochrones have their turn-offs at the tip of the stellar locus with the sub-giant branch and RGB being ‘folded’ towards redder regions of this color space. Utilizing this method we obtained a sample of 2554 nMSTO stars among the 4 fields, which corresponds to  $\sim 388$  stars/deg<sup>2</sup>, doubling the abundance of our RGB sample.

### 3.3. Distances

Photometric distances for both tracers were estimated by employing PARSEC (Bressan et al. 2012) isochrones. The selection of isochrones must cover both the metallicity distribution function and the age ranges that are expected to be found in the MW halo.

Particularly for the MW halo, An et al. (2013) found the metallicity distribution function to peak at  $[M/H] \simeq -1.7$  and  $-2.3$ . Alternatively, Conroy et al. (2019) found that the mean halo metallicity to be  $[Fe/H] \simeq -1.2$ , displaying no gradient between 6 – 100 kpc.

Since our RGB selection imposes an upper limit in the metallicity of  $[M/H] \simeq -1.3$ , we will utilize a flat halo prior that includes isochrones with a metallicity range of  $[M/H] \simeq -1.3$  to  $-2$ . The ages pose a secondary role, as metallicity has a larger impact on the inferred distances (Conroy et al. 2021). For completeness, we chose to include isochrones with ages from 10 – 12 Gyr, which takes into account most of the MW halo age distribution (Xiang & Rix 2022; Jofré & Weiss 2011).

The observed apparent  $g$  magnitude and the absolute magnitude from the isochrone, at a given  $(g-i)$  color, were used to derive the distance modulus between each tracer and each of the isochrones in the grid. The final distance for each tracer was calculated as the average distance modulus across the entire isochrone grid, thus computing distances without preference for any population, and incorporating the uncertainty associated with this choice.

Utilizing the previously computed distances, we selected a total of 102 giants and 309 nMSTO stars between 60 - 100 kpc in Galactocentric distance, that will be used in subsequent analysis. Of the RGB sample 5, 17, 32 and 48 are found in Tiles 1, 2, 3 and 4 respectively, for the nMSTO sample 44, 54, 94 and 117 are found in Tiles 1, 2, 3 and 4 respectively.

## 4. STELLAR DENSITY PROFILES

### 4.1. Density variations across the wake

All of our four fields are aligned at DEC = 0°, hence we can present a projected density profile by comparing the stellar counts for each tracer (nMSTO and RGB stars) with respect to their Right Ascension (RA). Based on Garavito-Camargo et al. (2019) simulations, the range of RA spanned by the 4 observed fields will cover the full density range that is expected to be found for the wake stellar overdensity.

To define a zero point for the density profiles, we integrated the halo best-fit radial density profile according to Xue et al. (2015), which corresponds to an Einasto profile (Einasto 1965) of  $n = 3.1 \pm 0.5$ , with an effective radius  $r_{\text{eff}} = 15 \pm 2$  kpc and a flattening of  $q = 0.7 \pm 0.02$  defined as follows:

$$\rho_*(r_q) \equiv \rho_0 \exp[-d_n[(r_q/r_{\text{eff}})^{(1/n)} - 1]] \quad (2)$$

where  $d_n \approx 3n - 1/3 + 0.0079/n$ ;  $r_q = \sqrt{R^2 + (z/q(r))^2}$  is the basic Galactocentric radial coordinate given the flattening  $q(r)$ , the Galactocentric radius  $R$  and the

Galactic coordinate  $z$ ;  $\rho_0$  corresponds to the normalization parameter.

To determine the normalization constant, we integrate Equation 2 over the entire sky from 1 to 45 kpc, calculating the stellar halo mass within this volume. This result is then compared with the mass estimates for the same region derived by Bell et al. (2008), illustrated in the equation below:

$$M_{\text{halo}}/\rho_0 = \int_1^{45} \int_0^{2\pi} \int_{-\frac{\pi}{2}}^{\frac{\pi}{2}} r_q^2 \cos(b) \rho(r_q) db dl dr_q \quad (3)$$

Where  $M_{\text{halo}}$  corresponds to the stellar halo mass contained between 1-45 kpc from the Galactic center, the factor  $r_q^2 \cos(b)$  is the Jacobian determinant for the transformation to spherical coordinates. By comparing the result of Eq. 3 to the mass of the Milky Way halo between 1 and 45 kpc, as determined in Bell et al. (2008) to be  $3.7 \pm 1.2 \times 10^8 M_\odot$ , we get a normalization constant  $\rho_0 \approx (4.5 \pm 1.5) \times 10^{19} M_\odot/\text{pc}^3$ .

Now we can compute the expected mass of the Milky Way halo between 60 and 100 kpc, where the density contrast and therefore the signature of the wake is expected to be the highest (Garavito-Camargo et al. 2019). Integrating Equation 2 with the previously found value of  $\rho_0$ , we get an outer halo stellar mass between 60 – 100 kpc of  $\approx (2.9 \pm 0.9) \times 10^7 M_\odot$ . This mass estimate includes stars of all evolutionary states. Therefore, a mass-to-number ratio for nMSTO and RGB stars is needed to compute an expected average number of sources for each of our tracers, which will be used later to obtain an average background stellar halo density with respect to which observed density contrasts will be computed and discussed.

Using PARSEC 1.2s tracks (Bressan et al. 2012), we simulated a 10 Gyr-old stellar population with a metallicity of -1.5 dex, corresponding to the peak of the halo metallicity distribution function and age distribution. This simulation drew from a Kroupa initial mass function, corrected for non-resolved binaries (Kroupa 2001; Kroupa et al. 2013), and a total mass of  $10^5 M_\odot$  given the limits of the code. We can then obtain a mass-to-number ratio by applying our color selection criteria presented in Section 3, to the simulated photometry output in SDSS  $g$ ,  $i$  and 2MASS  $K_s$  bands and dividing the resulting number of stars by the known total mass of the simulated population. This procedure yielded mass-to-number ratio estimates of  $149.7 M_\odot/\text{star}$  for nMSTO stars and  $343.4 M_\odot/\text{star}$  for RGB stars. Given these ratios and the previously determined stellar mass of the halo between 60 – 100 kpc, we get an estimated  $12 \pm 4$  giants and  $28 \pm 9$  nMSTO stars for each field, which will

represent the average stellar halo background density (i.e.,  $\bar{\rho}$ , see Equation 4) in Figure 7. This accounts for roughly 1/2.45 of our observed sample between 60-100 kpc (1/2.76 of our nMSTO sample and 1/2.1 of the giants sample), which includes 102 giants and 309 nMSTO stars.

Figure 7 illustrates the density profile in RA at DEC=0°, integrated between the line of sight and considering only stars found between 60 and 100 kpc from the Galactic center. The changes in the local density ( $\Delta\rho$ ) are measured for each tracer as shown in equation 4, where the measured number of stars between 60 and 100 kpc ( $\rho$ ) is divided by the previously computed average number density ( $\bar{\rho}$ ) of the entire MW halo, according to the best-fit Einasto profile by Xue et al. (2015). The dark matter particle number density of the Garavito-Camargo et al. (2019) simulation, including the formation of a DM wake owing to the first infall orbit of a  $2.5 \times 10^{11} M_\odot$  LMC, is presented in light blue and normalized to the  $\bar{\rho}$  of the entire halo of the simulation.

$$\Delta\rho = \rho/\bar{\rho} - 1. \quad (4)$$

Figure 7 presents a clear overdensity, consistent between both tracers, showing the maximum measured density in Tile 4 at RA  $\sim 335$  deg with an average overdensity of  $\Delta\rho = 3.1 \pm 0.7$ . The lowest density is measured for Tile 1 at RA  $\sim 7$  deg for both nMSTO and RGB stars. Although both tracers exhibit a similar trend of decreasing density from Tile 4 to Tile 1, the densities measured by each tracer become inconsistent at the  $1\sigma$  level in Tile 1, likely due to the low number of stars present in the RGB sample (5 stars) in Tile 1.

We perform a Z-test (Upton & Cook 2008) to probe the significance of these variations in density as a function of the RA coordinate. The null hypothesis is that of a hierarchically formed spherical halo, without the influence of the LMC. This hypothesis is grounded in the concept that Milky Way-like galaxies evolve through the hierarchical growth process, involving mergers and accretion of smaller systems. These systems, once influenced by the MW's tidal gravitational field, become progressively more mixed. This process eventually leads to the formation of a spheroidal component of the halo, a result of their collective assembly, with a significant portion of it constituted by in-homogeneous substructures such as streams, plumes, and dwarf satellite galaxies (Searle & Zinn 1978; Bullock & Johnston 2005; Abadi et al. 2006; De Lucia 2012; Re Fiorentin et al. 2015; Monachesi et al. 2019).

For this purpose, we look at the simulated halos of Bullock & Johnston (2005), which are entirely hierarchically constituted. Since in their simulations the halo

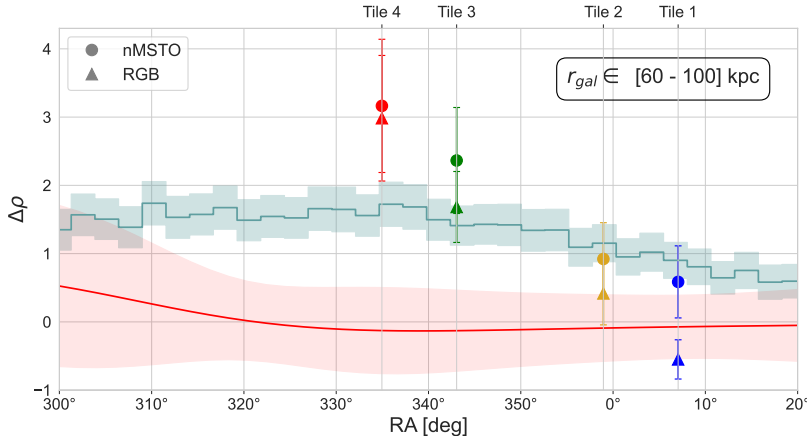


**Figure 7.** Derived density profile  $\Delta\rho$ , integrated along the line-of-sight between 60-100 kpc from the Galactic center and projected as a function of RA. The number density of nMSTO stars is indicated as points, and the density of RGB stars is shown as downward pointing triangles, for both the color is dependant on the corresponding Tile, with red, green, yellow, and blue for Tiles 1, 2, 3 and 4. Both tracers are normalized according to the best-fit Einasto profile by Xue et al. (2015), as described in the text. The light blue histogram represents the number density profile of dark matter for the same segment of the halo between 60-100 kpc, from the Garavito-Camargo et al. (2019) model including the formation of a wake owing to the passage of the LMC with a virial mass at infall of  $2.5 \times 10^{11} M_{\odot}$ , normalized by the average density ( $\bar{\rho}$ ) in the entire sky of the simulation. Error bars, shown in light blue, reflect 1000 bootstraps of the slice, encompassing the same DEC as the observed fields. A kernel density estimate of the average relative number density profile in RA for three random DEC coordinates in all Bullock & Johnston (2005) halos is shown in red, with the surrounding lighter red area corresponding to the  $1\sigma$  dispersion. A clear density enhancement is observed for both nMSTO and RGB stars, peaking at Tile 4, as expected from the simulation.

is spherical and therefore it could be considered to be no preferred direction in the outer halo, we considered 3 random stripes with a major axis equal in length to the angular range shown in Figure 7 and a minor axis equal to the angular size of a VIRCAM field of view ( $1.64 \text{ deg}^2$  Emerson et al. 2006), and selected stellar particles between 60 and 100 kpc from the Galactic center. The mean kernel density estimate for  $\Delta\rho$  is almost constant around zero and the mean standard deviation found across all 11 Bullock & Johnston (2005) halos is on average  $\overline{\sigma_{bj}} = 0.59$ . Therefore, the null hypothesis for the Z-test is that the observed relative densities follow a flat distribution with a mean of zero and a standard deviation of 0.59. The Z-score for the highest density field (Tile 4) is 5.02 and 5.32 for RGB and nMSTO stars respectively, which corresponds to a p-value of  $\sim 0$ . Thus passing the 95% significance test. We can therefore consider this detection to have  $> 5\sigma$  significance.

#### 4.2. Radial Density Profiles

An analysis of the radial density profile facilitates the detection of substructures along the line of sight (Pila-Díez et al. 2015; Xue et al. 2015). Additionally, Garavito-Camargo et al. (2019) predicts a measurable footprint of the wake in the radial density profile. To construct the radial density profile for the more abundant nMSTO stars, they are split into 8 bins by their Galactocentric radius between 20 - 100 kpc, we then

calculate the number density per bin and line of sight ( $\rho_{l,b,r}$ ) as follows:

$$\rho_{l,b,r} = \frac{N_{l,b,r}}{V} \quad (5)$$

Where  $V$  corresponds to the volume contained within each galactocentric bin ( $r_1, r_1 + 7.27 \text{ kpc}$ ) computed by integrating the solid angle of the observed field with the corresponding heliocentric distance  $r_h$  that results in the corresponding bin.

$$V = \int_{\theta_1}^{\theta_2} \int_{\phi_1}^{\phi_2} \int_{r_1}^{r_2} r_h(\theta, \phi, r_{gc})^2 \cos(\phi) J dr_{gal} d\phi d\theta \quad (6)$$

Where  $r_1$  and  $r_2$  correspond to the minimum and maximum Galactocentric radii of the bin, respectively;  $\theta_1$ ,  $\phi_1$  and  $\theta_2$ ,  $\phi_2$  are the spherical coordinates covered by the observed field centered at the galactic center and aligned with the Galactic coordinate system convention, and  $r_h(\theta, \phi, r_{gc})$  is the heliocentric radius expressed as a function of the coordinates  $\theta$ ,  $\phi$ , and the Galactocentric radius  $r_{gc}$ , defined by:

$$r_h(r_g, \theta, \phi) = R_0 \cos(\theta) \cos(\phi) + \sqrt{r_g^2 + R_0^2 \cos^2(\theta) \cos^2(\phi) - R_0^2} \quad (7)$$

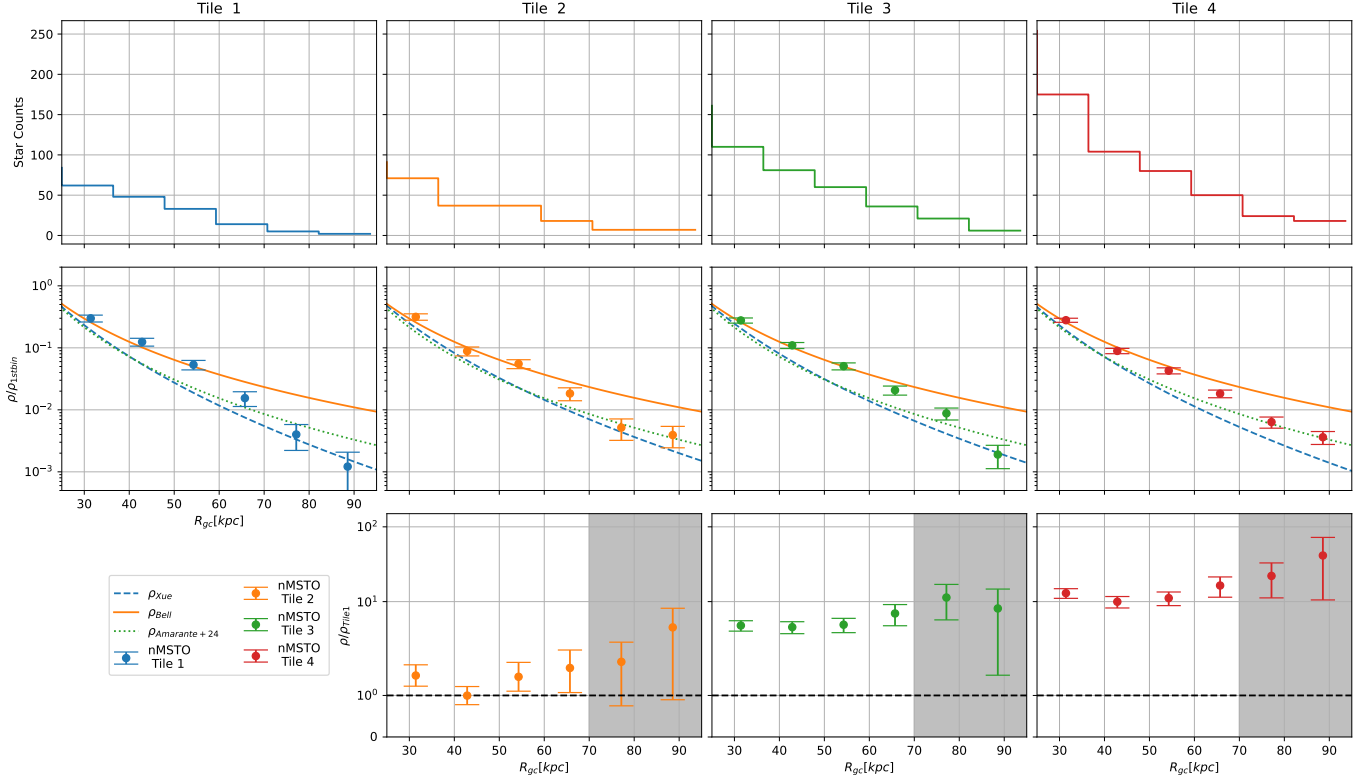


**Figure 8.** First-row shows the star counts as a function of galactocentric radius for nMSTO stars. The second row shows the stellar density profiles for the nMSTO stars for the 4 observed fields (ie., the first row divided by volume), normalized according to the number density of the highest density bin at 25 kpc (just after the expected position of the break in the halo), thus bypassing the computation of an error-prone normalization parameter for each radial density profile and allowing comparison in the slope. Xue et al. (2015), Bell et al. (2008) and Amarante et al. (2024) radial density profiles are shown as blue, orange, and green lines, respectively. nMSTO radial density is shown in blue, orange, green, and red corresponding to Tiles 1,2,3, and 4, this holds for the entire plot. The third row shows the radial density profiles relative to Tile 1. Error bars correspond to Poisson errors. We find our data closely resembles Bell et al. (2008) radial density profile up to  $\sim 70$  kpc where Xue et al. (2015) profile shows a better agreement. There is an increase in density with respect to Tile 1 that increases further at 70 kpc.

While  $J$  is the jacobian of the transformation from Galactocentric radius to heliocentric radius, given by:

$$dr_h = \frac{r_g dr_g}{\sqrt{r_g^2 + R_0^2 \cos^2(\theta) \cos^2(\phi) - R_0^2}} \quad (8)$$

$$\equiv J,$$

where  $R_0$  is the distance between the Sun and the Galactic Center. Computing the volume for each bin in this way allows us to compensate for the deviation between the solid angle observed on our line of sight and the center of the shell defined by each bin, i.e., for the fact that we are not observing from the Galactic Center.

The results of the number density calculations are presented in Figure 8, where the nMSTO stellar counts are shown as a function of the Galactocentric distance  $R_{gc}$  for each Tile (shown in the upper row of panels of Figure 8). These number counts are then divided by the volume of each bin and normalized to the maximum density bin (which corresponds to the bin at 25 kpc), thus produc-

ing the radial density profile shown in the middle row of panels of Figure 8. The normalization allows for a comparison between the shapes of published stellar halo profiles and our data, as each profile requires a scaling factor to fit the data. For reference, recall that Tile 1 (leftmost panel) corresponds to the lowest density measured along our pointings, and Tile 4 (rightmost panel) to the peak density, for tracers between 60 – 100 kpc (Figure 7). The triaxial broken-power law density profile from Bell et al. (2008) is shown as an orange curve, along with the Einasto profile from Xue et al. (2015) in blue, labeled as  $\rho_{\text{Bell}}$  and  $\rho_{\text{Xue}}$ , respectively.

Figure 8 illustrates that the density profiles decrease as a function of Galactocentric radius in all tiles, consistent with Bell et al. (2008) triaxial double power-law model only up to 60 – 70 kpc. Beyond this point, a discontinuity and change in slope is observed, where our data appears to be better explained by Xue et al. (2015) Einasto profile. The apparent deviation from the Bell



profile in all tiles beyond  $\sim 60$  kpc is very suggestive of a real change, as this happens to be the distance regime at which the LMC wake is expected to manifest (Garavito-Camargo et al. 2019). This change in the halo density profile after  $\sim 60$  kpc becomes very clear in Figure 9, where we stack the data of all our pointings, as discussed ahead.

From Figure 2, our fiducial simulation predicts a density gradient across the 4 tiles, where Tile 1 should be the least dense relative to the other tiles, and Tile 4 should be the most dense. This was confirmed in projection in Figure 7. We now examine the behavior of this relative density enhancement as a function of Galactocentric distance. We achieve this by dividing (bin by bin) the observed stellar densities of Tiles 2, 3, and 4 by the corresponding ones observed for Tile 1. This produces, as shown in the bottom row of panels of Figure 8, observed halo density profiles relative to a field in the outskirts of the wake, for three adjacent sight lines that go, across the sky, into the expected location of the peak of the LMC wake. The trend of increasing density from Tile 2 to 4 now appears clearly. Moreover, in Tiles 2, 3, and 4 there are hints of a jump in the stellar density relative to Tile 1 that starts at  $\sim 70$  kpc and that increases in magnitude across the sky, peaking in Tile 4. Such an increasing density gradient across the sky (Tiles 1 to 4) and that jumps starting at  $\sim 70$  kpc is consistent with the predictions from the simulations of Garavito-Camargo et al. (2019). Importantly, the angular scale over which our density profile displays the density jump (Tile 1 – 4 = 32.5 degrees) is larger than the expected angular scale subtended by substructure in hierarchically constituted halo simulations (see 5.2).

Additionally, for Tiles 3 and 4 we observe an increasing density contrast at small distances as well (between 20 - 70 kpc), which maintains the same  $\rho_{\text{Bell}}$  slope but at higher star counts. This behavior indicates that the halo in this region of the sky may be highly anisotropic and thus non-spherical (see Woudenbergh & Helmi 2024). Alternatively, within 70 kpc this could be due to the presence of contamination from Sagittarius, even though our fields are at higher latitudes than where the main track from the Sagittarius stream is.

Finally, in order to confirm or reject the reality of a new density break observed in all Tiles between  $\sim 60$ –70 kpc and better determine its location, we combined the data from all 4 Tiles in order to boost the star counts, which allows the construction of a density profile with a better spatial resolution (i.e., with bins of 2.5 kpc instead of 10 kpc). We fit this combined radial density profile with a triaxial double power law using a Monte Carlo Markov Chain (MCMC) approach, which yields

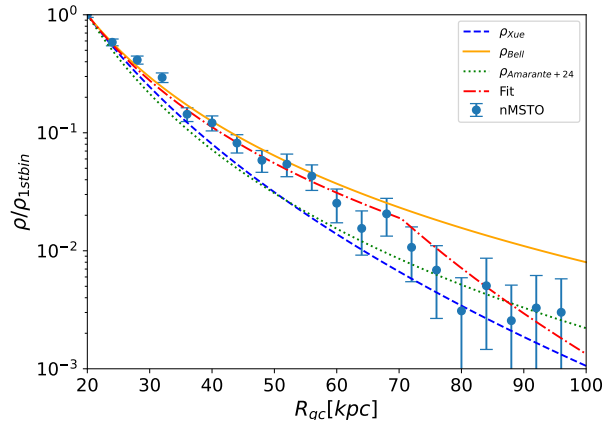


**Figure 9.** The combined radial density profile for all four tiles shows the nMSTO number density normalized by the density of the first bin, enabling a comparison of slopes. The radial density profiles from Xue et al. (2015), Bell et al. (2008), and Amarante et al. (2024) are represented by a blue dashed line, an orange solid line, and green dots, respectively. Our double power law fit for the nMSTO radial profile is depicted as a red dot-dashed line. The break that was apparent in the middle row of panels of Figure 8 is now significantly more clear, with best-fit value at  $67.5^{+4.8}_{-5.0}$  kpc.

a best fit of  $\alpha_{in} = 3.13^{+0.48}_{-0.61}$ ,  $\alpha_{out} = 7.46^{+0.44}_{-0.53}$ , with a break radius of  $67.5^{+4.8}_{-5.0}$  kpc, and presented in Figure 9 with a dot-dashed red line. The MCMC simultaneously fits the triaxiality ratios, for which we found  $b/a = 1.0^{+0.57}_{-0.44}$  and  $c/a = 0.98^{+0.49}_{-0.50}$ . Since the data from our fields was combined the resulting  $b/a$  and  $c/a$  ratios representing the triaxiality were not constrained as this would require simultaneously fitting the profile in different directions of the sky.

## 5. DISCUSSION

In this section, we discuss our findings on the characterization of the overdensity that we identify as the wake in the Galactic halo, and the implications for understanding the density profile of the outer halo.

### 5.1. Comparison with other studies

Conroy et al. (2021) reported the first detection of the wake and the collective response, through an all-sky approach to probe the MW halo using K giants and RR Lyrae stars. This was achieved using data from Gaia (Gaia Collaboration et al. 2023) and WISE (Wright et al. 2010) all-sky surveys. Their findings indicated that the local wake’s density contrast exceeded the predictions by Garavito-Camargo et al. (2019) by a factor of  $1.4 \pm 0.2$  and  $2.1 \pm 0.3$ , for K giants and RR Lyrae, respectively. Our study, finds an overdensity that exceeds Garavito-Camargo et al. (2019) predictions by a factor

of  $1.8 \pm 0.4$ , consistent between the K giants and nMSTO tracers.

Amarante et al. (2024) employed Legacy Survey DR9 (Dey et al. 2019) photometry to identify a large sample of BHB stars that reach distances of 120 kpc. They do not find a statistically significant detection of the collective response in density. However, they report a signature that they identify with the wake through a density contrast  $\geq 0.6$ , measured across a region that is 60 degrees long, 25 degrees wide, and aligned with the LMC’s orbit. They find a radial density profile that follows a double power law but with a break radius and internal/external slopes that vary depending on the direction of the sky (see their figure 7). This also supports a non-spherical anisotropic stellar halo, in line with our findings presented in Section 4.2. In particular for the direction of the wake they fit a double power law to the radial density profile that does not constrain the break radius, which suggests that the break at 70 kpc could also be present in their data.

Throughout all these studies, therefore, a detectable wake overdensity is measured with a statistical significance above  $5\sigma$  in a consistent position in the sky.

## 5.2. Contamination and Substructure

Hierarchical formation models of the MW predict the formation of a spheroidal halo as a result of the assembly of accreted progenitors (Searle & Zinn 1978; Helmi et al. 1999; Bullock & Johnston 2005; Abadi et al. 2006; Gómez & Helmi 2010; De Lucia 2012; Re Fiorentin et al. 2015). Several prominent over-densities have already been detected at distances beyond 50 kpc (Sesar et al. 2007; Watkins et al. 2009; Belokurov et al. 2019). Additionally, there is the case of the Gaia Sausage/Enceladus (GS/E) merger - an ancient interaction between the young MW and a large dwarf galaxy (Belokurov et al. 2018; Helmi et al. 2018). This merger is estimated to have taken place between 8-11 Gyr ago (Myeong et al. 2018; Helmi et al. 2018). During the interaction, the GS/E progenitor’s orbit radialized quickly, and the satellite sunk to the bottom of the Galactic potential well and fell apart, flooding the inner halo with its tidal debris (Amorisco 2017; Naidu et al. 2021; Belokurov et al. 2018; Helmi et al. 2018).

However, the earliest bouts of tidal stripping likely resulted in stars being unbound from the GS/E progenitor at much larger distances, when the dwarf began engaging with the Galaxy. Numerical simulations show that these earlier stripped stars remain coherent in the outer halo for a couple of dynamical times (Amorisco 2017), particularly in the distance range probed in this study. This same mechanism applies to other ac-

creted satellites, therefore, we expect the outer halo to be composed of coherent substructures (Bullock & Johnston 2005; Gómez et al. 2013), whose density variations could display a wake-like footprint. In fact, Chandra et al. (2023b) suggests that at least 20% and up to 50% of the Pisces Plume is composed of unmixed debris from the Clouds.

As shown in Section 4.1, considering Bullock & Johnston (2005) halo models (constructed entirely of substructure) as the null hypothesis for a Z test, our wake detection passes the statistical significance test above 95%, therefore the likelihood that the overdensity reported is the result of substructure is low. However, it is possible that chance alignments of substructure-induced overdensities could reproduce the density enhancements observed, but for this to be the case they must have the same angular size scale as the overdensity we observe, i.e., cover at least 30 degrees.

The left panel in Figure 10 shows the distribution of angular scales for substructures identified in the halos modeled by Bullock & Johnston (2005). In this context, we define substructures as overdensities without requiring a shared origin for the constituent particles. See Appendix B for a detailed explanation of the procedure used to identify and measure the angular scale of the substructures.

We found that 35.2% of the substructures identified had an angular scale equal to or larger than the angular scale covered by our observations. Among these substructures, the majority are streams or alignments of stream-like features (see right panel of Figure 10 for an example of one of the identified substructures). A characteristic trait of streams is that, when observed through a narrow field, they typically reside at a specific distance from the Galactic center. This would manifest as an excess in the radial density profile at that particular radius, which is not evident in most of our data, as it can be seen in Figure 8.

However, Chandra et al. (2023a) discovered through a spectroscopic survey of K giants in the halo, that the Pisces overdensity is composed of 20-50% debris from the Clouds. If this proportion is at the upper limit, accounting for the debris contribution would align both our detection and the findings of Conroy et al. (2021) with Garavito-Camargo et al. (2019) models. Given the density contrast observed in Figure 7, reducing it by subtracting potential contamination would, even at the upper limit, maintain a density contrast consistent with a massive LMC.

The only known substructure that could induce significant contamination in the region of the sky covered by our fields is the Sagittarius stellar stream. As previ-

ously mentioned, it could explain the increased density observed within 60 kpc, even though our fields are at higher latitudes than the main track of the Sagittarius stream. Specifically, the two most likely fields to be contaminated are Tile 1 and Tile 2, as they are closer to the main track of Sagittarius according to the [Vasiliev et al. \(2021\)](#) catalog. If Tile 1 and Tile 2 were significantly contaminated by the Sagittarius stream, it would imply that the density contrast observed in the line of sight, when using Tile 1 as a comparison, is larger than shown in Figure 8 and that the density differential presented in Figure 7 would also be larger than shown.

## 6. SUMMARY AND CONCLUSIONS

We obtained wide-field deep optical and near-infrared imaging with the DECam and VIRCAM instruments, respectively, in four fields covering the region of the Southern sky expected to show a stellar density enhancement in the Galactic halo due to the presence of the dynamical friction wake caused by the passage of the LMC (e.g., [Garavito-Camargo et al. 2019](#)). These data reach significantly fainter levels than previous surveys that cover this region, allowing us to map distant regions of the MW halo with good number statistics (provided by faint tracers), and using two different stellar tracers. Taking advantage of  $(g - i)$ ,  $(i - K_S)$  color-color selections, an efficient and reliable star/background galaxy separation is achieved in regions of the CMD previously prohibited by the high levels of confusion (see Section 2.4 and Figure 3). We obtain samples of 102 K giants and 309 nMSTO stars spanning Galactocentric distances between 60 – 100 kpc. Our analysis of these datasets has revealed the following:

- The radial stellar halo density profile in the region we examine is consistent with the outer slope of the double power-law fit by [Bell et al. \(2008\)](#), which was derived using MSTO stars from SDSS imaging. However, this agreement holds only up to a distance of 60 – 70 kpc from the Galactic center (Figure 8). Beyond this range, the density profile becomes steeper across all our fields, aligning more closely with the Einasto-like profile identified by [Xue et al. \(2015\)](#) using K giants from the SEGUE survey. It is worth noting that both [Bell et al. \(2008\)](#) and [Xue et al. \(2015\)](#) focused on the Galactic halo as observed from the Northern hemisphere. When we combine the nMSTO stars from all sightlines, this transition becomes more pronounced, revealing a clear break radius at approximately 70 kpc, deep in the distant halo (Figure 9).
- The integrated number of halo stars with Galactocentric distances between 60 – 100 kpc steadily increases across the sky with increasing Right Ascension (Figure 7, going from our Tile 1 to Tile 4), which corresponds to moving across the Southern sky into the expected current location of the LMC wake according to numerical simulations. Both stellar tracers used, K giants and nMSTO stars, show this same behavior, in qualitative and quantitative terms.
- The maximum density enhancement observed in our data, relative to a smooth local halo, occurs in the easternmost of our fields, which prevents us from determining whether we have reached the actual peak of the overdensity associated with the LMC wake. The density contrast at this maximum is  $\Delta\rho = 3.1 \pm 0.7$ , corresponding to roughly four times the average density of a smooth local halo, as estimated in Section 4.1. This overdensity is more pronounced than predicted by any current models of the LMC wake and is slightly larger than the value reported by [Conroy et al. \(2021\)](#) from their all-sky analysis using K giants, though it remains within the error bars of their RR Lyrae measurement.
- As a function of Galactocentric distance, the radial halo density profiles, normalized to that of our field farthest from the wake (Figure 8), show a density contrast/enhancement beyond 70 kpc that steadily increases as we move across the sky towards the expected current location of the LMC wake, as predicted by simulations. This result is consistent with the findings from the integrated star counts.
- At closer distances (20-60 kpc), where models of the LMC infall do not predict a significant contribution from the wake, we still observe an enhancement in the radial density profiles relative to our reference field (the field farthest from the wake’s location in the sky). This enhancement is small near the reference field but increases rapidly towards the east, in the direction of the projected wake location. Since current models do not expect the LMC wake to influence the inner regions of the stellar halo as covered by our data, these excesses may suggest the presence of substructure from other origins or a highly anisotropic, non-spherical halo in these regions of the sky.
- The peak overdensity in distant stellar halo counts, as measured in our data, exceeds the predictions

from all Garavito-Camargo et al. (2019) models. To match the observed peak, it would require an LMC mass greater than  $2.5 \times 10^{11} M_{\odot}$ , the highest virial mass at infall tested in their models, and/or a slightly different LMC orbit.

Most of the findings summarized above regarding the distant Galactic stellar halo in the direction of our fields align with predictions from current numerical simulations of the LMC’s infall towards the Milky Way (Garavito-Camargo et al. 2019). This provides strong evidence that the overdensity observed in our survey corresponds to the stellar wake trailing the LMC during its first passage through the halo. However, the observed strength of the overdensity surpasses that of all available models, suggesting that the LMC may be more massive than other independent estimates suggest. Additionally, the observed density enhancements could potentially be influenced by other forms of halo substructure in the region we probed. The presence of some contamination is further supported by the identification of stellar debris from the LMC and SMC in the Pisces Plume region (Chandra et al. 2023a), as well as by the excess we observe at distances closer than the current location of the Clouds.

This work has explored the distant MW stellar halo down to photometric depths previously unprobed in the Southern hemisphere through wide-field observations. Future studies with broader area coverage will be essential for further characterizing the LMC wake and disentangling potential contamination from other substructures in this region. In particular, more detailed investigations of the LMC wake and halo substructure will be enabled by upcoming surveys such as LSST (Ivezić et al. 2019), which will provide multiband photometry

and proper motion data for much of the Southern hemisphere. When combined with radial velocities and chemical abundances from spectroscopic surveys like SDSS-V (Kollmeier et al. 2017), DESI (DESI Collaboration et al. 2023) and WEAVE (Jin et al. 2023), these data will offer a comprehensive, multidimensional view of the Milky Way’s halo. This will improve our understanding of the Galaxy’s assembly, the mass and orbital elements of its more massive satellites, and ultimately allow the use of their interactions as a test for dark matter models and gravity itself.

#### ACKNOWLEDGEMENTS

We thank Kathryn Johnston, Manuela Zoccali, Javier Alonso, Roberto Muñoz, Rogelio Albarracín, Aquiles den Braber, Camila Aravena, Alvaro Valenzuela, Eitan Dvorkoz and Julio Olivares for the insightful discussions. MC and JC acknowledge support from the Agencia Nacional de Investigación y Desarrollo (ANID) via Proyecto Fondecyt Regular 1191366 and 1231345, and by ANID BASAL project FB210003. CN acknowledges support by the Centre National d’études Spatiales (CNES). G.B. is supported by NSF CAREER AST1941096. FAG acknowledges funding from the Max Planck Society through a “PartnerGroup” grant. FAG acknowledges support from ANID FONDECYT Regular 1211370, the ANID Basal Project FB210003 and the HORIZON-MSCA-2021-SE-01 Research and innovation programme under the Marie Skłodowska-Curie grant agreement number 101086388. The Geryon cluster at the Centro de Astro-Ingeniería UC was extensively used for the calculations performed in this work. ANID BASAL project FB21000, BASAL CATA PFB-06, the Anillo ACT-86, FONDEQUIP AIC-57, and QUIMAL 130008 provided funding for several improvements to the Geryon cluster.

#### REFERENCES

- Abadi, M. G., Navarro, J. F., & Steinmetz, M. 2006, *MNRAS*, 365, 747, doi: [10.1111/j.1365-2966.2005.09789.x](https://doi.org/10.1111/j.1365-2966.2005.09789.x)
- Abbott, T. M. C., Adamów, M., Aguena, M., et al. 2021, *ApJS*, 255, 20, doi: [10.3847/1538-4365/ac00b3](https://doi.org/10.3847/1538-4365/ac00b3)
- Ahumada, R., Allende Prieto, C., Almeida, A., et al. 2020, *ApJS*, 249, 3, doi: [10.3847/1538-4365/ab929e](https://doi.org/10.3847/1538-4365/ab929e)
- Amarante, J. A. S., Kuposov, S. E., & Laporte, C. F. P. 2024, arXiv e-prints, arXiv:2404.09825, doi: [10.48550/arXiv.2404.09825](https://doi.org/10.48550/arXiv.2404.09825)
- Amorisco, N. C. 2017, *MNRAS*, 464, 2882, doi: [10.1093/mnras/stw2229](https://doi.org/10.1093/mnras/stw2229)
- An, D., Beers, T. C., Johnson, J. A., et al. 2013, *ApJ*, 763, 65, doi: [10.1088/0004-637X/763/1/65](https://doi.org/10.1088/0004-637X/763/1/65)
- Angelov, T. 1996, *Bulletin Astronomique de Belgrade*, 154, 13
- Bell, E. F., Zucker, D. B., Belokurov, V., et al. 2008, *ApJ*, 680, 295, doi: [10.1086/588032](https://doi.org/10.1086/588032)
- Belokurov, V., Deason, A. J., Erkal, D., et al. 2019, *MNRAS*, 488, L47, doi: [10.1093/mnras/513/l47](https://doi.org/10.1093/mnras/513/l47)
- Belokurov, V., Erkal, D., Evans, N. W., Kuposov, S. E., & Deason, A. J. 2018, *MNRAS*, 478, 611, doi: [10.1093/mnras/sty982](https://doi.org/10.1093/mnras/sty982)
- Bertin, E. 2011, in *Astronomical Society of the Pacific Conference Series*, Vol. 442, *Astronomical Data Analysis Software and Systems XX*, ed. I. N. Evans, A. Accomazzi, D. J. Mink, & A. H. Rots, 435



- Bertin, E., & Arnouts, S. 1996, *A&AS*, 117, 393, doi: [10.1051/aas:1996164](https://doi.org/10.1051/aas:1996164)
- Bertin, E., Mellier, Y., Radovich, M., et al. 2002, in *Astronomical Society of the Pacific Conference Series*, Vol. 281, *Astronomical Data Analysis Software and Systems XI*, ed. D. A. Bohlender, D. Durand, & T. H. Handley, 228
- Besla, G., Kallivayalil, N., Hernquist, L., et al. 2007, *ApJ*, 668, 949, doi: [10.1086/521385](https://doi.org/10.1086/521385)
- . 2010, *ApJL*, 721, L97, doi: [10.1088/2041-8205/721/2/L97](https://doi.org/10.1088/2041-8205/721/2/L97)
- Bond, N. A., Ivezić, Ž., Sesar, B., et al. 2010, *ApJ*, 716, 1, doi: [10.1088/0004-637X/716/1/1](https://doi.org/10.1088/0004-637X/716/1/1)
- Bressan, A., Marigo, P., Girardi, L., et al. 2012, *MNRAS*, 427, 127, doi: [10.1111/j.1365-2966.2012.21948.x](https://doi.org/10.1111/j.1365-2966.2012.21948.x)
- Bullock, J. S., & Johnston, K. V. 2005, *ApJ*, 635, 931, doi: [10.1086/497422](https://doi.org/10.1086/497422)
- Campello, R. J. G. B., Moulavi, D., & Sander, J. 2013, in *Advances in Knowledge Discovery and Data Mining*, Vol. 7819 (Springer), 1 – 52
- Campello, R. J. G. B., Moulavi, D., Zimek, A., & Sander, J. 2015, *ACM Trans. Knowl. Discov. Data*, 10, doi: [10.1145/2733381](https://doi.org/10.1145/2733381)
- Canny, J. 1986, *IEEE Transactions on Pattern Analysis and Machine Intelligence*, PAMI-8, 679, doi: [10.1109/TPAMI.1986.4767851](https://doi.org/10.1109/TPAMI.1986.4767851)
- Cappellari, M., McDermid, R. M., Alatalo, K., et al. 2013, *MNRAS*, 432, 1862, doi: [10.1093/mnras/stt644](https://doi.org/10.1093/mnras/stt644)
- Chandra, V., Naidu, R. P., Conroy, C., et al. 2023a, *ApJ*, 956, 110, doi: [10.3847/1538-4357/acf7bf](https://doi.org/10.3847/1538-4357/acf7bf)
- . 2023b, *ApJ*, 951, 26, doi: [10.3847/1538-4357/accf13](https://doi.org/10.3847/1538-4357/accf13)
- . 2024, *arXiv e-prints*, arXiv:2406.01676, doi: [10.48550/arXiv.2406.01676](https://doi.org/10.48550/arXiv.2406.01676)
- Chandrasekhar, S. 1943, *ApJ*, 97, 255, doi: [10.1086/144517](https://doi.org/10.1086/144517)
- Chen, B., Stoughton, C., Smith, J. A., et al. 2001, *ApJ*, 553, 184, doi: [10.1086/320647](https://doi.org/10.1086/320647)
- Cleveland, W. S., & Devlin, S. J. 1988, *Journal of the American Statistical Association*, 83, 596, doi: [10.1080/01621459.1988.10478639](https://doi.org/10.1080/01621459.1988.10478639)
- Conroy, C., Naidu, R. P., Garavito-Camargo, N., et al. 2021, *Nature*, 592, 534, doi: [10.1038/s41586-021-03385-7](https://doi.org/10.1038/s41586-021-03385-7)
- Conroy, C., Naidu, R. P., Zaritsky, D., et al. 2019, *ApJ*, 887, 237, doi: [10.3847/1538-4357/ab5710](https://doi.org/10.3847/1538-4357/ab5710)
- Correa Magnus, L., & Vasiliev, E. 2022, *MNRAS*, 511, 2610, doi: [10.1093/mnras/stab3726](https://doi.org/10.1093/mnras/stab3726)
- Cui, X.-Q., Zhao, Y.-H., Chu, Y.-Q., et al. 2012, *Research in Astronomy and Astrophysics*, 12, 1197, doi: [10.1088/1674-4527/12/9/003](https://doi.org/10.1088/1674-4527/12/9/003)
- Dalton, G. B., Caldwell, M., Ward, A. K., et al. 2006, in *Society of Photo-Optical Instrumentation Engineers (SPIE) Conference Series*, Vol. 6269, *Society of Photo-Optical Instrumentation Engineers (SPIE) Conference Series*, ed. I. S. McLean & M. Iye, 62690X, doi: [10.1117/12.670018](https://doi.org/10.1117/12.670018)
- De Lucia, G. 2012, *Astronomische Nachrichten*, 333, 460, doi: [10.1002/asna.201211683](https://doi.org/10.1002/asna.201211683)
- Deason, A. J., Belokurov, V., Koposov, S. E., & Lancaster, L. 2018, *ApJL*, 862, L1, doi: [10.3847/2041-8213/aad0ee](https://doi.org/10.3847/2041-8213/aad0ee)
- DESI Collaboration Et Al. 2023, *The Early Data Release of the Dark Energy Spectroscopic Instrument*, Zenodo, doi: [10.5281/ZENODO.7964161](https://doi.org/10.5281/ZENODO.7964161)
- Dey, A., Schlegel, D. J., Lang, D., et al. 2019, *AJ*, 157, 168, doi: [10.3847/1538-3881/ab089d](https://doi.org/10.3847/1538-3881/ab089d)
- Einasto, J. 1965, *Trudy Astrofizicheskogo Instituta Alma-Ata*, 5, 87
- Emerson, J., McPherson, A., & Sutherland, W. 2006, *The Messenger*, 126, 41
- Emerson, J. P., Irwin, M. J., Lewis, J., et al. 2004, in *Society of Photo-Optical Instrumentation Engineers (SPIE) Conference Series*, Vol. 5493, *Optimizing Scientific Return for Astronomy through Information Technologies*, ed. P. J. Quinn & A. Bridger, 401–410, doi: [10.1117/12.551582](https://doi.org/10.1117/12.551582)
- Erkal, D., & Belokurov, V. A. 2020, *MNRAS*, 495, 2554, doi: [10.1093/mnras/staa1238](https://doi.org/10.1093/mnras/staa1238)
- Erkal, D., Belokurov, V., Laporte, C. F. P., et al. 2019, *MNRAS*, 487, 2685, doi: [10.1093/mnras/stz1371](https://doi.org/10.1093/mnras/stz1371)
- Erkal, D., Deason, A. J., Belokurov, V., et al. 2021, *MNRAS*, 506, 2677, doi: [10.1093/mnras/stab1828](https://doi.org/10.1093/mnras/stab1828)
- Fabricius, C., Luri, X., Arenou, F., et al. 2021, *A&A*, 649, A5, doi: [10.1051/0004-6361/202039834](https://doi.org/10.1051/0004-6361/202039834)
- Flaugher, B., Diehl, H. T., Honscheid, K., et al. 2015, *AJ*, 150, 150, doi: [10.1088/0004-6256/150/5/150](https://doi.org/10.1088/0004-6256/150/5/150)
- Foote, H. R., Besla, G., Mocz, P., et al. 2023, *The Astrophysical Journal*, 954, 163, doi: [10.3847/1538-4357/ace533](https://doi.org/10.3847/1538-4357/ace533)
- Furlanetto, S. R., & Loeb, A. 2002, *ApJ*, 565, 854, doi: [10.1086/324693](https://doi.org/10.1086/324693)
- Gaia Collaboration, Vallenari, A., Brown, A. G. A., et al. 2023, *A&A*, 674, A1, doi: [10.1051/0004-6361/202243940](https://doi.org/10.1051/0004-6361/202243940)
- Garavito-Camargo, N., Besla, G., Laporte, C. F. P., et al. 2019, *ApJ*, 884, 51, doi: [10.3847/1538-4357/ab32eb](https://doi.org/10.3847/1538-4357/ab32eb)
- . 2021, *ApJ*, 919, 109, doi: [10.3847/1538-4357/ac0b44](https://doi.org/10.3847/1538-4357/ac0b44)
- Gómez, F. A., Besla, G., Carpintero, D. D., et al. 2015, *ApJ*, 802, 128, doi: [10.1088/0004-637X/802/2/128](https://doi.org/10.1088/0004-637X/802/2/128)
- Gómez, F. A., & Helmi, A. 2010, *MNRAS*, 401, 2285, doi: [10.1111/j.1365-2966.2009.15841.x](https://doi.org/10.1111/j.1365-2966.2009.15841.x)

- Gómez, F. A., Helmi, A., Cooper, A. P., et al. 2013, *MNRAS*, 436, 3602, doi: [10.1093/mnras/stt1838](https://doi.org/10.1093/mnras/stt1838)
- Gruen, D., Seitz, S., & Bernstein, G. M. 2014, *PASP*, 126, 158, doi: [10.1086/675080](https://doi.org/10.1086/675080)
- Helmi, A., Babusiaux, C., Koppelman, H. H., et al. 2018, *Nature*, 563, 85, doi: [10.1038/s41586-018-0625-x](https://doi.org/10.1038/s41586-018-0625-x)
- Helmi, A., White, S. D. M., de Zeeuw, P. T., & Zhao, H. 1999, *Nature*, 402, 53, doi: [10.1038/46980](https://doi.org/10.1038/46980)
- Irwin, M. J., Lewis, J., Hodgkin, S., et al. 2004, in *Society of Photo-Optical Instrumentation Engineers (SPIE) Conference Series*, Vol. 5493, *Optimizing Scientific Return for Astronomy through Information Technologies*, ed. P. J. Quinn & A. Bridger, 411–422, doi: [10.1117/12.551449](https://doi.org/10.1117/12.551449)
- Ivezić, Ž., Sesar, B., Jurić, M., et al. 2008, *ApJ*, 684, 287, doi: [10.1086/589678](https://doi.org/10.1086/589678)
- Ivezić, Ž., Kahn, S. M., Tyson, J. A., et al. 2019, *ApJ*, 873, 111, doi: [10.3847/1538-4357/ab042c](https://doi.org/10.3847/1538-4357/ab042c)
- Jin, S., Trager, S. C., Dalton, G. B., et al. 2023, *Monthly Notices of the Royal Astronomical Society*, 530, 2688–2730, doi: [10.1093/mnras/stad557](https://doi.org/10.1093/mnras/stad557)
- Jofré, P., & Weiss, A. 2011, *A&A*, 533, A59, doi: [10.1051/0004-6361/201117131](https://doi.org/10.1051/0004-6361/201117131)
- Jurić, M., Ivezić, Ž., Brooks, A., et al. 2008, *ApJ*, 673, 864, doi: [10.1086/523619](https://doi.org/10.1086/523619)
- Kallivayalil, N., van der Marel, R. P., & Alcock, C. 2006a, *ApJ*, 652, 1213, doi: [10.1086/508014](https://doi.org/10.1086/508014)
- Kallivayalil, N., van der Marel, R. P., Alcock, C., et al. 2006b, *ApJ*, 638, 772, doi: [10.1086/498972](https://doi.org/10.1086/498972)
- Kollmeier, J. A., Zasowski, G., Rix, H.-W., et al. 2017, *arXiv e-prints*, arXiv:1711.03234, doi: [10.48550/arXiv.1711.03234](https://doi.org/10.48550/arXiv.1711.03234)
- Koposov, S. E., Belokurov, V., Torrealba, G., & Evans, N. W. 2015, *ApJ*, 805, 130, doi: [10.1088/0004-637X/805/2/130](https://doi.org/10.1088/0004-637X/805/2/130)
- Koposov, S. E., Erkal, D., Li, T. S., et al. 2023, *MNRAS*, 521, 4936, doi: [10.1093/mnras/stad551](https://doi.org/10.1093/mnras/stad551)
- Kroupa, P. 2001, in *Astronomical Society of the Pacific Conference Series*, Vol. 228, *Dynamics of Star Clusters and the Milky Way*, ed. S. Deiters, B. Fuchs, A. Just, R. Spurzem, & R. Wielen, 187, doi: [10.48550/arXiv.astro-ph/0011328](https://doi.org/10.48550/arXiv.astro-ph/0011328)
- Kroupa, P., Weidner, C., Pflamm-Altenburg, J., et al. 2013, in *Planets, Stars and Stellar Systems. Volume 5: Galactic Structure and Stellar Populations*, ed. T. D. Oswalt & G. Gilmore, Vol. 5 (Springer Netherlands), 115, doi: [10.1007/978-94-007-5612-0\\_4](https://doi.org/10.1007/978-94-007-5612-0_4)
- Lancaster, L., Giovanetti, C., Mocz, P., et al. 2020, *JCAP*, 2020, 001, doi: [10.1088/1475-7516/2020/01/001](https://doi.org/10.1088/1475-7516/2020/01/001)
- Lawrence, A., Warren, S. J., Almaini, O., et al. 2013, *VizieR Online Data Catalog*, II/319
- Matas, J., Galambos, C., & Kittler, J. 2000, *Computer Vision and Image Understanding*, 78, 119, doi: [10.1006/cviu.1999.0831](https://doi.org/10.1006/cviu.1999.0831)
- McInnes, L., Healy, J., & Astels, S. 2017, *The Journal of Open Source Software*, 2, doi: [10.21105/joss.00205](https://doi.org/10.21105/joss.00205)
- McMahon, R. G., Banerji, M., Gonzalez, E., et al. 2013, *The Messenger*, 154, 35
- Meingast, S., Alves, J., Mardones, D., et al. 2016, *A&A*, 587, A153, doi: [10.1051/0004-6361/201527160](https://doi.org/10.1051/0004-6361/201527160)
- Monachesi, A., Gómez, F. A., Grand, R. J. J., et al. 2019, *MNRAS*, 485, 2589, doi: [10.1093/mnras/stz538](https://doi.org/10.1093/mnras/stz538)
- Muñoz, R. P., Puzia, T. H., Lançon, A., et al. 2014, *ApJS*, 210, 4, doi: [10.1088/0067-0049/210/1/4](https://doi.org/10.1088/0067-0049/210/1/4)
- Myeong, G. C., Evans, N. W., Belokurov, V., Sanders, J. L., & Koposov, S. E. 2018, *ApJL*, 863, L28, doi: [10.3847/2041-8213/aad7f7](https://doi.org/10.3847/2041-8213/aad7f7)
- Naidu, R. P., Conroy, C., Bonaca, A., et al. 2021, *ApJ*, 923, 92, doi: [10.3847/1538-4357/ac2d2d](https://doi.org/10.3847/1538-4357/ac2d2d)
- Nie, J. D., Smith, M. C., Belokurov, V., et al. 2015, *ApJ*, 810, 153, doi: [10.1088/0004-637X/810/2/153](https://doi.org/10.1088/0004-637X/810/2/153)
- Ordenes-Briceño, Y., Puzia, T. H., Eigenthaler, P., et al. 2018, *ApJ*, 860, 4, doi: [10.3847/1538-4357/aac1b8](https://doi.org/10.3847/1538-4357/aac1b8)
- Ostriker, J. P. 1999, *ApJ*, 525C, 297
- Patel, E., Besla, G., & Sohn, S. T. 2017, *MNRAS*, 464, 3825, doi: [10.1093/mnras/stw2616](https://doi.org/10.1093/mnras/stw2616)
- Peñarrubia, J., Gómez, F. A., Besla, G., Erkal, D., & Ma, Y.-Z. 2016, *MNRAS*, 456, L54, doi: [10.1093/mnrasl/slv160](https://doi.org/10.1093/mnrasl/slv160)
- Petersen, M. S., & Peñarrubia, J. 2021, *Nature Astronomy*, 5, 251, doi: [10.1038/s41550-020-01254-3](https://doi.org/10.1038/s41550-020-01254-3)
- Pila-Díez, B., de Jong, J. T. A., Kuijken, K., van der Burg, R. F. J., & Hoekstra, H. 2015, *A&A*, 579, A38, doi: [10.1051/0004-6361/201425457](https://doi.org/10.1051/0004-6361/201425457)
- Re Fiorentin, P., Lattanzi, M. G., Spagna, A., & Curir, A. 2015, *AJ*, 150, 128, doi: [10.1088/0004-6256/150/4/128](https://doi.org/10.1088/0004-6256/150/4/128)
- Riello, M., De Angeli, F., Evans, D. W., et al. 2021, *A&A*, 649, A3, doi: [10.1051/0004-6361/202039587](https://doi.org/10.1051/0004-6361/202039587)
- Rockosi, C. M., Lee, Y. S., Morrison, H. L., et al. 2022, *ApJS*, 259, 60, doi: [10.3847/1538-4365/ac5323](https://doi.org/10.3847/1538-4365/ac5323)
- Rozier, S., Famaey, B., Siebert, A., et al. 2022, *ApJ*, 933, 113, doi: [10.3847/1538-4357/ac7139](https://doi.org/10.3847/1538-4357/ac7139)
- Schlafly, E. F., & Finkbeiner, D. P. 2011, *ApJ*, 737, 103, doi: [10.1088/0004-637X/737/2/103](https://doi.org/10.1088/0004-637X/737/2/103)
- Schlegel, D. J., Finkbeiner, D. P., & Davis, M. 1998, *ApJ*, 500, 525, doi: [10.1086/305772](https://doi.org/10.1086/305772)
- Searle, L., & Zinn, R. 1978, *ApJ*, 225, 357, doi: [10.1086/156499](https://doi.org/10.1086/156499)

- Sesar, B., Jurić, M., & Ivezić, Ž. 2011, *ApJ*, 731, 4,  
doi: [10.1088/0004-637X/731/1/4](https://doi.org/10.1088/0004-637X/731/1/4)
- Sesar, B., Ivezić, Ž., Lupton, R. H., et al. 2007, *AJ*, 134,  
2236, doi: [10.1086/521819](https://doi.org/10.1086/521819)
- Shipp, N., Erkal, D., Drlica-Wagner, A., et al. 2021, *ApJ*,  
923, 149, doi: [10.3847/1538-4357/ac2e93](https://doi.org/10.3847/1538-4357/ac2e93)
- Tamfal, T., Mayer, L., Quinn, T. R., et al. 2021, *ApJ*, 916,  
55, doi: [10.3847/1538-4357/ac0627](https://doi.org/10.3847/1538-4357/ac0627)
- Upton, G., & Cook, I. 2008, *A Dictionary of Statistics*, 2nd  
edn. (Oxford University Press),  
doi: [10.1093/acref/9780199541454.001.0001](https://doi.org/10.1093/acref/9780199541454.001.0001)
- Valdes, F., Gruendl, R., & DES Project. 2014, in  
*Astronomical Society of the Pacific Conference Series*,  
Vol. 485, *Astronomical Data Analysis Software and  
Systems XXIII*, ed. N. Manset & P. Forshay, 379
- Vasiliev, E. 2024, *MNRAS*, 527, 437,  
doi: [10.1093/mnras/stad2612](https://doi.org/10.1093/mnras/stad2612)
- Vasiliev, E., Belokurov, V., & Erkal, D. 2021, *MNRAS*, 501,  
2279, doi: [10.1093/mnras/staa3673](https://doi.org/10.1093/mnras/staa3673)
- Vioque, M., Cavierres, M., González, M. P., et al. 2023, *AJ*,  
166, 183, doi: [10.3847/1538-3881/acf75f](https://doi.org/10.3847/1538-3881/acf75f)
- Vitsos, A., & Gourgouliatos, K. N. 2023, *JCAP*, 2023, 071,  
doi: [10.1088/1475-7516/2023/04/071](https://doi.org/10.1088/1475-7516/2023/04/071)
- Watkins, L. L., Evans, N. W., Belokurov, V., et al. 2009,  
*MNRAS*, 398, 1757,  
doi: [10.1111/j.1365-2966.2009.15242.x](https://doi.org/10.1111/j.1365-2966.2009.15242.x)
- Woudenberg, H. C., & Helmi, A. 2024, *arXiv e-prints*,  
*arXiv:2407.21790*, doi: [10.48550/arXiv.2407.21790](https://doi.org/10.48550/arXiv.2407.21790)
- Wright, E. L., Eisenhardt, P. R. M., Mainzer, A. K., et al.  
2010, *AJ*, 140, 1868, doi: [10.1088/0004-6256/140/6/1868](https://doi.org/10.1088/0004-6256/140/6/1868)
- Xiang, M., & Rix, H.-W. 2022, *Nature*, 603, 599,  
doi: [10.1038/s41586-022-04496-5](https://doi.org/10.1038/s41586-022-04496-5)
- Xue, X.-X., Rix, H.-W., Ma, Z., et al. 2015, *ApJ*, 809, 144,  
doi: [10.1088/0004-637X/809/2/144](https://doi.org/10.1088/0004-637X/809/2/144)
- Yaaqib, R., Petersen, M. S., & Peñarrubia, J. 2024,  
*MNRAS*, 531, 3524, doi: [10.1093/mnras/stae1363](https://doi.org/10.1093/mnras/stae1363)

## APPENDIX

## A. COEFFICIENTS FOR THE STAR/GALAXY SEPARATION

Polynomial best-fit found for the star/galaxy separation procedure described in Section 2.4.

$$\begin{aligned}
 i - Ks = & - 8.90365315 \times 10^{-4}(g - i)^6 \\
 & + 5.40619658 \times 10^{-3}(g - i)^5 \\
 & + 6.25122688 \times 10^{-3}(g - i)^4 \\
 & - 4.85818006 \times 10^{-2}(g - i)^3 \\
 & - 0.116253605(g - i)^2 \\
 & + 1.04653713(g - i) \\
 & - 0.961426796
 \end{aligned} \tag{A1}$$

## B. ANGULAR SCALE OF SUBSTRUCTURES

The definition of substructure relevant to this article refers to overdensities in the halo up to approximately 100 kpc. Thus, the identification of substructures in the halos modeled by [Bullock & Johnston \(2005\)](#) could not rely on particle IDs, as we are also interested in overdensities caused by the alignment of progenitors.

For this reason, we utilized the implementation from [McInnes et al. \(2017\)](#) of HDBSCAN: Hierarchical Density-Based Spatial Clustering of Applications with Noise ([Campello et al. 2013, 2015](#)) to identify substructures through clustering. We choose to use HDBSCAN as it is density-based and not biased towards any particular density range or shape of the structures, thus allowing for the identification of substructures with different spatial morphologies (e.g., streams, plumes, shells, clouds, dwarf galaxies )

The X, Y and Z coordinates of each particle between 60 - 100 kpc were scaled to have a median of zero and interquartile unit range, such that HDBSCAN is not biased towards any coordinate or direction.

We then run HDBSCAN using the two main clustering parameters `min_samples = 350`, `min_cluster_size = 350`, as we found that the typical substructure tends to have at least 350 members, and choosing a lower number that would increase sensitivity tends to fragment clusters into smaller ones, which in turn would artificially bias the angular scale distribution towards smaller substructure. The last user set parameter of importance is `cluster_selection_method`, for which we utilized `'leaf'` (see [McInnes et al. \(2017\)](#)).

As we are interested in projected densities, we then merge any cluster that has members with a projected angular distance of less than 5 degrees. This also allows us to deal with fragmented clusters and streams. See [Figure 10](#) which shows the projected particles between 60-100 kpc from the Galactic center in a [Bullock & Johnston \(2005\)](#) simulation and shows the morphology of a typical overdensity detected by HDBSCAN.

Finally, the angular scale of a given cluster is computed following [Vioque et al. \(2023\)](#) definition of the radius that contains 80% of the cluster members, this angular scale should therefore be considered as the angular scale of the cluster in their most elongated way.

The previously described procedure is applied to all [Bullock & Johnston \(2005\)](#) halos to construct the angular scale distribution shown on panel a) in [Figure 10](#).



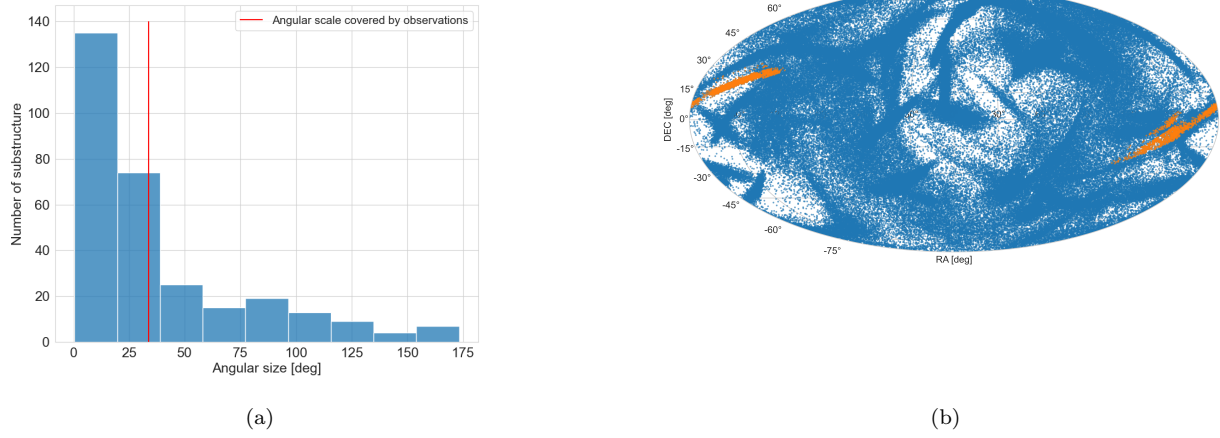


**Figure 10.** Panel (a) displays the angular scale distribution of overdensities across the 11 [Bullock & Johnston \(2005\)](#) halo models, where the angular scale is defined as the radius from the geometrical center that contains 80% of the particles. This radius is oriented along the most elongated direction of the structure ([Vioque et al. 2023](#)). Panel (b) shows a Mollweide projection of particles between 60-100 kpc in the 11th [Bullock & Johnston \(2005\)](#) halo model, highlighting an example of a merged cluster in orange, with other particles shown in blue, to illustrate the presence of many substructures within this halo.